Title

Mesoscopic modeling of transport resistances in a polymer-electrolyte fuel-cell catalyst layer: Analysis of hydrogen limiting currents

Authors

Mu, Yu-Tong
Weber, Adam Z
Gu, Zhao-Lin
et al.

Publication Date

2019-12-01

DOI

10.1016/j.apenergy.2019.113895

Mesoscopic Modeling of Transport Resistances in a Polymer-Electrolyte Fuel-Cell Catalyst Layer: Analysis of Hydrogen Limiting Currents

Yu-Tong Mu [a], Adam Z. Weber [b], Zhao-Lin Gu [a], and Wen-Quan Tao [c*]
a. School of Human Settlements and Civil Engineering, Xi'an Jiaotong University, Xi'an, Shaanxi, 710054, China
b. Energy Conversion Group, Energy Technologies Area, Lawrence Berkeley National Laboratory, 1 Cyclotron Road, Berkeley CA 94720, USA
c. Key Laboratory of Thermo-Fluid Engineering and Science of MOE, School of Energy and Power Engineering, Xi'an Jiaotong University, Xi'an, Shaanxi, 710049, China
*Corresponding email: wqtao@xjtu.edu.cn

Understanding transport resistances in a polymer-electrolyte fuel cell (PEFC) catalyst layer (CL) is essential to mitigate the unexpected voltage loss when using low loadings of precious metals. In this paper, we explore through mesoscopic modeling the quantification analyses of the transport resistances in CL as derived using hydrogen-pump limiting current. Numerical treatments on the conjugated interfacial conditions at interfaces of ionomer/pore and Pt/ionomer are proposed to describe the mesoscopic transport processes of hydrogen and proton. Characterizations of the reconstructed microstructure of CL are performed. Parameter analyses on the influences of the critical transport properties such as the permeation coefficient and the dissolution and adsorption reaction rates at the surfaces of ionomer/pore and Pt/ionomer on the local transport resistance are presented. It is found that the local transport resistance is mainly originated from the diffusion resistance of the ionomer thin-film, which is more resistive than its bulk analogue with its permeation coefficient fitted to be 5.9% of the bulk one. The interfacial transport resistances and the diffusion resistance are coupled. The local transport resistance increases with I/C ratio due to thicker ionomer coated on the particles. Higher Pt/C ratio and bare carbon fraction lead to higher local transport resistance since the ionomer loading relative to Pt roughness factor decreases. The local transport resistance decreases with the porosity. The contribution of pores to the CL resistance, which decreases with the porosity, is comparatively small at low loadings.

Keywords: PEFC, Local transport resistance, Low-loaded platinum, Catalyst layer, Lattice Boltzmann method

1. Introduction

A polymer-electrolyte fuel cell (PEFC) has been commonly regarded as a promising energy-conversion device that converts the chemical energy stored in hydrogen to electrical energy directly [1]. Considerable attentions have been received due to its benefits including the remarkable high efficiency at a comparatively low operating temperature [2] and the low emissions to the environment [3]. Nevertheless, the worldwide commercialization of the PEFC is highly challenged by its relatively expensive cost [4]. Therefore, reducing the platinum (Pt) amount in the membrane-electrode-assembly (MEA) without sacrificing its performance is of particular importance. As widely reported in several critical reviews [5-7] that a significant and unacceptable performance loss exists as the Pt loading (L_{Pt}) decreases. Detailed analyses provided by Greszler et al. [8] revealed that a local transport resistance of oxygen ($R_{\mathrm{O_2}}^{\mathrm{Pt}}$) in the catalyst layer (CL) accounted for the voltage loss. The measured $R_{\mathrm{O_2}}^{\mathrm{Pt}}$ is in the range of 100 to 1000 $\mathrm{s \cdot m^{-1}}$, which is an order-of-magnitude higher than that expected, possibly due to the transport through the ionomer thin-film [9]. Thus, understanding the genesis of $R_{\mathrm{O_2}}^{\mathrm{Pt}}$ is critical for the optimization of Pt utilization and CL performance at low L_{Pt}.

The hypothesis that transport properties of the reactant species in the ionomer thin-film are highly reduced compared with its bulk due to confinement effects [10] or substrate interactions [11] has led to attempts to characterize the morphology of the ionomer thin-film. Phase-separation as the film thickness approaching 20 nm was observed [12], leading to changes in its properties such as surface wettability and water uptake [13], swelling [14], mechanical properties [9], and transition temperature [15]. Given that $R_{\mathrm{O_2}}^{\mathrm{Pt}}$ is dominated by the diffusion resistance of the ionomer thin-film, it should vary linearly with the film thickness. Suzuki et al. [16] measured the thickness-dependent resistance of Nafion, and observed a positive non-zero intercept resistance, indicating the existence of an interfacial transport resistance. Owejan et al. [17] analyzed $R_{\mathrm{O_2}}^{\mathrm{Pt}}$ with different Pt dispersions and concluded that the interfacial transport resistance dominated the observed performance loss. Kudo et al. [18] found that the interfacial resistance was equivalent to the ionomer thickness of 30 to 70 nm. To distinguish the origins of the interfacial resistance from the interfacial surfaces of Pt/ionomer and ionomer/pore, Liu et al. [19] measured the thickness-dependent $R_{\mathrm{O_2}}^{\mathrm{Pt}}$ and concluded that there was no interfacial transport resistance at the ionomer/gas interface. Suzuki et al. [20] measured the potential-dependent transport resistance in the CL, and attributed $R_{O_2}^{Pt}$ to the sulfonate coverage of the effective Pt surfaces. Recent molecular-dynamics studies revealed that $R_{O_2}^{Pt}$ was dominated by the oxygen permeation at the Pt/ionomer interface since the adsorption between the sulfonate groups and Pt hinders the oxygen transport [21]. Apart from the ionomer thin-film, liquid water in the CL is also regarded as a possible genesis of $R_{O_2}^{Pt}$. When cells operate at high current density, the impact of water production and electro-osmotic drag may result in the water flooding in cathode, thereby hindering the oxygen transport to the reaction sites [22]. This has been evidenced by Nonoyama et al. [23] that $R_{O_2}^{Pt}$ increased with higher relative humidity (over 100%). Muzaffar et al. [24] analyzed L_{Pt} dependent physical properties of CL and believed that the tipping water balance dominated the massive transport loss. Mashio et al. [25] attributed $R_{O_2}^{Pt}$ to two local transport processes including the gas transport through the ionomer and the liquid water.

Generally, owing to the complicated transport phenomena in the cathode CL, factors such as the possible existence of oxide formation, production of water and heat, together with their coupled influence on the effective transport properties make the traditional oxygen-limiting-current measurement complicated. Attention thus turns to the local transport resistance of hydrogen ($R_{H_2}^{Pt}$) to mimic $R_{O_2}^{Pt}$ due to its simplicity and deconvoluted mechanisms. Spingler et al. [26] experimentally measured $R_{H_2}^{Pt}$ with a hydrogen-pump technique and concluded that the mass-dependent transport resistance through the ionomer thin-film was limiting. Freiberg et al. [27] further validated the diffusion-dominated origin of $R_{H_2}^{Pt}$ with the hydrogen-limiting-current measurement. Recently, Schuler et al. [28] concluded that the majority of the CL resistance was ascribed to $R_{H_2}^{Pt}$ consisting of the interfacial and bulk-type diffusion resistances. They found that the non-mass-dependent interfacial resistance was about a third of the diffusion resistance.

Compared with the experimental measurement of the local transport resistance, analytical models in the framework of the agglomerate model have been developed to explore the transport processes in the CL. Moore et al. [29] and Kulikovsky [30] respectively integrated the interfacial transport resistance at the ionomer/pore and Pt/ionomer interfaces into the agglomerate model. Schuler et al. [28] and Hao et al. [31] considered the Pt distribution on the agglomerate surface and further extended the above model to consider the 2-D mass transport by introducing a focusing factor. Jiang et al. [32] employed the agglomerate model to study the performance of the ordered electrode. Zhang et al. [33]

recently explored the degradation of the agglomerates on the reactive transport process. A comprehensive review of the existing ten analytical models for transport resistance has been performed by Darling [34]. He concluded that most of the models, failing to describe the real 3-D transport processes of the reactant species from pores to the catalytic sites, did not match the empirically observed trends when applied to predict the variations of the transport resistance versus the structural parameters. Only the one incorporating nanoparticle limitation and localized diffusion or adsorption on the platinum particles showed a relative satisfactory trend. However, the large and random critical parameters such as the agglomerate size and the film thickness widely used in the agglomerate model were not supported in scanning electron micrographs (SEM) [35, 36], which may not give a clue to improve the CL structure.

The mesoscale or microstructural models performed on the actual structure of the CL can be regarded as a better approach since they can capture the detailed transport and reaction details occurring in the heterogeneous and complex structures. Cetinbas et al. [37] and Lange et al. [38] performed a mesoscopic analysis on the 3-D microstructure of the CL and evaluated the effective transport properties of proton and oxygen. Zhang et al. [39] and Sabharwal et al. [40] focused on the oxygen diffusion and dissolution processes in the CL. However, the work performed by Zhang et al. [39] was actually based on the agglomerate model without distinguishing the components of Pt and carbon, and the electrochemical reaction was taking place everywhere inside the solid phase. The work conducted by Sabharwal et al. [40] also did not take into account the ionomer morphology. The ionomer with constant thickness was assumed to be located at the gas-solid interfaces and the reaction rate was corrected with the ratio of the active area of platinum and the total areas of the gas-solid interfaces. Chen et al. [41] and Siddique and Liu [42] studied the coupled transport process inside the reconstructed microstructures of the CL with all the four components considered. Hou et al. [43] recently investigated the structural parameters on the CL performance and proposed an ideal catalyst layer structure.

Indeed, the local transport processes of the reactant species permeating from pores to ionomer thin-films before reaching Pt surfaces possibly include the following processes: gas transport in pores, dissolution from pores to ionomer thin-film, permeation in ionomer thin-film, adsorption at the ionomer/Pt interfaces, and chemical reactions at the ionomer-Pt-carbon surfaces. As not all the ionomer-Pt-carbon surfaces are served as the reaction site, the transport process of proton in ionomer thin-film should be taken into account. However, few mesoscopic studies focused on the local transport resistance of the reactant gases with all the above transport processes included, and none of them further considered the additional possible interfacial resistances by including both the dissolution resistance (R_{dis}) and the adsorption resistance (R_{ads}) at mesoscopic level simultaneously. The objective of the present work is to develop a mesoscopic numerical method, which can fully consider all the transport details of hydrogen and proton in a CL undergoing a hydrogen-limiting-current diagnostic. With this model, transport resistances are numerically characterized and compared with the existing experimental data. In addition, the influences of the structural parameters of the CL on the transport resistances are explored. It is believed that the present mesoscopic method is instructive for the design and optimization of the CL at low L_{Pt}.

2. Methods

To explore the local transport resistances, simulations are performed that mimic the hydrogen-limiting-current experiments of Weber and coworkers [26-28, 44] as shown in Fig. 1. In their experiments, the reference electrode with a constant L_{Pt} of 0.4 mg·cm^{-2} and the working electrode with L_{Pt} ranging from 0.03 to 0.4 mg·cm^{-2} were deposited on a membrane (MEM). MEM was sandwiched between the gas-diffusion layers (GDL). Diluted argon mixtures were fed to the cell with 2% H_2/Ar in the reference electrode and 1000 ppm H_2/Ar in the working electrode. The limiting-current experiments were executed at 40°C and 90% RH with a backpressure of 1 atm. The total transport resistance of hydrogen (R_{tot}) is calculated as

$$R_{\mathrm{tot}} = \frac{2Fc_{\mathrm{H_2,bulk}}}{i_{\mathrm{lim}}} = R_{\mathrm{CH}} + R_{\mathrm{GDL}} + R_{\mathrm{CL}} \tag{1}$$

where i_{lim}, F, $c_{\mathrm{H2,bulk}}$, R_{CH}, R_{GDL}, and R_{CL} are the limiting current density, Faraday's constant, the bulk concentration of hydrogen, and the transport resistances in channel, GDL and CL, respectively. R_{CL} can be further expressed as [8],

$$R_{\mathrm{CL}} = \frac{R_{\mathrm{H_2}}^{\mathrm{Pt}}}{f_{\mathrm{Pt}}}\left(l/\psi\right)\coth\left(l/\psi\right) \tag{2}$$

where l and f_{Pt} are the CL thickness and roughness factor, respectively. The quantity ψ is defined as $\psi = \sqrt{D_{\mathrm{H_2}}^{\mathrm{eff}} l R_{\mathrm{H_2}}^{\mathrm{Pt}} / f_{\mathrm{Pt}}}$ with $D_{\mathrm{H_2}}^{\mathrm{eff}}$ denoted as the effective hydrogen diffusivity in CL. One can find that the contribution of pores and ionomer thin-film to R_{CL} are fully coupled. As l/ψ approaches zero, Eq. (2) can be further simplified with the Taylor-series expansion [28],

$$R_{\mathrm{CL}} = \frac{l}{3D_{\mathrm{H_2}}^{\mathrm{eff}}} + \frac{R_{\mathrm{H_2}}^{\mathrm{Pt}}}{f_{\mathrm{Pt}}} \tag{3}$$

The first term in the right hand side of Eq. (3) is denoted as R_{Pore}, reflecting the contribution of pores to R_{CL}. Typically, a plot of R_{CL} versus $1/f_{\mathrm{Pt}}$ can produce a straight line with a slope of $R_{\mathrm{H_2}}^{\mathrm{Pt}}$. By changing the carbon dilution or the CL thickness, a set of f_{Pt} can be acquired. However, for constant carbon dilution, the intercept $l/3D_{\mathrm{H_2}}^{\mathrm{eff}}$ also changes with f_{Pt}; while for constant CL thickness, $R_{\mathrm{H_2}}^{\mathrm{Pt}}$ changes with the carbon dilution [17]. Therefore, the accuracy of the predicted $R_{\mathrm{H_2}}^{\mathrm{Pt}}$ may be affected by the linear fitting method. To exclude the contribution of pores to R_{CL}, l should be sufficiently small or $D_{\mathrm{H_2}}^{\mathrm{eff}}$ should be comparatively high. Based on this idea, if the hydrogen concentration throughout the CL is the same, R_{Pore} can be neglected. Therefore, two steps are employed to obtain the values of $R_{\mathrm{H_2}}^{\mathrm{Pt}}$ and R_{Pore} for a given structure of the CL numerically: first, the hydrogen concentration throughout pores is assumed the same with that of the GDL/CL interface, the calculated R_{CL} is purely attributed to the ionomer thin-film. Therefore, $R_{\mathrm{H_2}}^{\mathrm{Pt}}$ can be easily calculated with the second term in the right hand side of Eq. (3); second, if the hydrogen transport process in the pores is included, R_{Pore} can be obtained simply by subtracting $R_{\mathrm{H_2}}^{\mathrm{Pt}}/f_{\mathrm{Pt}}$ from the newly calculated R_{CL}. Details on the calculation of f_{Pt} and R_{CL} will be addressed later. As $R_{\mathrm{H_2}}^{\mathrm{Pt}}$ is possibly ascribed to the contributions of R_{dis} at the interface of ionomer/pore, the diffusion resistance R_{I} through the ionomer thin-film and R_{ads} at the interface of Pt/ionomer [28], one has $R_{\mathrm{H_2}}^{\mathrm{Pt}} = R_{\mathrm{dis}} + R_{\mathrm{I}} + R_{\mathrm{ads}}$.

In the present work, only the CL of the working electrode is selected as the computational zone, and R_{GDL} is given as 35.16 $\mathrm{s \cdot m^{-1}}$ based on the GDL-stacking method in our previous work [28]. The value of R_{CH} is obtained based on the analyses given by Baker et al. [45] as $R_{\mathrm{CH}} = w\,(A_{\mathrm{CH}} + B_{\mathrm{CH}}\zeta)\,/D_{\mathrm{H2}}$ with the constants A_{CH} and B_{CH} given as 1.12 and 1.01, respectively. The dimensionless parameter $\zeta = L/(Pe \cdot w)$ is calculated with the Peclet number (Pe), channel width w and channel length L. Based on the experimental setup described in our previous experimental work [44], the calculated R_{CH} is 7.71 $\mathrm{s \cdot m^{-1}}$. The experiments are modeled using a mesoscopic approach, where numerically reconstructed microstructures of the CLs are used. The conjugated transport processes of hydrogen and proton in the microstructures of CLs, together with the electrochemical reactions, are solved with lattice Boltzmann method (LBM). Numerical treatments of the interfacial transport resistances at the interfaces of ionomer/pore and Pt/ionomer in the microstructure are proposed to characterize the possible origins of the local transport resistance.

Fig. 1 Schematic illustration of the transport processes of hydrogen in a hydrogen-limiting-current setup

2.1 Numerical method

With the present hydrogen-limiting-current technique, liquid water is not considered as no water is produced or consumed. Therefore, water content in the ionomer is assumed to be constant. As the hydrogen concentration in the working electrode is extremely small, the current density obtained is low and thus the isothermal assumption throughout the CL is valid. Since the conductivity of the electron is more than two orders of magnitude higher than that of the proton, electronic isopotential assumption is made [41]. Therefore, only the governing equations of the proton and hydrogen concentration are considered,

$$\nabla \cdot \left(\kappa \nabla \phi_{\mathrm{ion}} \right) + j = 0 \tag{4a}$$

$$\nabla \cdot \left(D \nabla c \right) + j_{\mathrm{H_2}} = 0 \tag{4b}$$

where c is the hydrogen concentration and ϕ is the proton (ionic) potential. Proton only transports in the ionomer phase and hydrogen transports in both pores and ionomer phases. All the sources terms in Eq. (4) only exists at the ionomer-Pt-carbon interfaces. The proton conductivity in the ionomer, κ, is expressed as [46]

$$\kappa = \frac{1}{2}\left(0.5139\lambda - 0.326\right)\exp\left[1268\left(\frac{1}{303} - \frac{1}{T}\right)\right] \tag{5}$$

with the water content λ calculated as a function of the water activity a [46],

$$\lambda = 0.043 + 17.18a - 39.85a^2 + 36a^3, \quad \left(0 < a = p_{\mathrm{vp}} / p_{\mathrm{sat}} < 1\right) \tag{6}$$

where p_{sat} and p_{vp} are denoted as the saturation water pressure and water vapor pressure, respectively.

As the typical pore size in the catalyst layer is around 100 nm, both molecular and Knudsen diffusion are considered to evaluate the hydrogen diffusivity D_p in the local pores of the CL,

$$D_\mathrm{p} = \left(\frac{1}{D_\mathrm{Kn}} + \frac{1}{D_{\mathrm{H_2:mix}}} \right)^{-1} \tag{7}$$

with the Knudsen diffusivity D_Kn calculated as

$$D_\mathrm{Kn} = \frac{2r}{3} \sqrt{\frac{8RT}{\pi M_{\mathrm{H_2}}}} \tag{8}$$

where r, R, M and T are the pore radius, universal gas constant, gas molecular weight, and absolute temperature, respectively. The molecular diffusivity for a binary mixture of gases is calculated with the Fuller-Schettler-Gidding equations [47],

$$D_{\mathrm{H_2:mix}} = \left(\frac{x_{\mathrm{H_2O}}}{D_{\mathrm{H_2:H_2O}}} + \frac{x_\mathrm{Ar}}{D_{\mathrm{H_2:Ar}}} \right)^{-1} \tag{9a}$$

$$D_{\mathrm{H_2:H_2O/Ar}} = \frac{0.001 T^{1.75}}{P\left(v_{\mathrm{H_2}}^{1/3} + v_{\mathrm{H_2O/Ar}}^{1/3}\right)^2} \left(\frac{1}{M_{\mathrm{H_2}}} + \frac{1}{M_{\mathrm{H_2O/Ar}}} \right)^{0.5} \tag{9b}$$

where P, x and v are the total pressure (unit of atm), mole fraction, and the diffusion volume of species, respectively. The diffusion volumes are 7.07, 16.1, and 12.7 $\mathrm{cm^3 \cdot mol^{-1}}$ for H_2, Ar, and H_2O, respectively [47].

At the interfaces of ionomer/pore, the hydrogen first dissolves into the ionomer with the equilibrium concentration of c_eq calculated by Henry's law,

$$c_\mathrm{eq} = \frac{RT}{H} c_\mathrm{p} \tag{10}$$

where c_p is the hydrogen concentration in gas phase. The Henry constant of hydrogen H (unit of $\mathrm{Pa \cdot (m^3 \cdot mol)^{-1}}$) is obtained as [36]

$$H = 0.101325 \times 0.255 \times 10^5 \exp(170/T) \tag{11}$$

As the hydrogen dissolution rate k_dis is limited, the dissolution transport resistance R_dis may exist. Correspondingly, the conjugated interfacial conditions can be expressed as

$$-D_{\mathrm{p}}\frac{\partial c_{\mathrm{p}}}{\partial \mathbf{n}}=-D_{\mathrm{ion}}\frac{\partial c_{\mathrm{ion}}}{\partial \mathbf{n}}=k_{\mathrm{dis}}\left(c_{\mathrm{eq}}-c_{\mathrm{ion}}\right) \tag{12}$$

where the diffusivity D_{ion} in the ionomer is calculated as $D_{\mathrm{ion}}=H\psi_0$ with the permeation coefficient ψ_0 (unit of mol·(m s Pa)$^{-1}$) given by [48]

$$\psi_0=\left(2.2\times10^{-14}f_{\mathrm{vp}}+2.9\times10^{-15}\right)\exp\left[\frac{21000}{R}\left(1/T-1/303.15\right)\right] \tag{13}$$

with f_{vp} the volume fraction of water in the vapor-equilibrated region of membrane.

Compared with the dual pathway kinetic approximation, the Tafel approximation may overestimate the hydrogen oxidation reaction (HOR) at low overpotentials. However, the present work mainly focuses on the diffusion-limited process near limiting current with the overpotentials higher than 0.3V throughout the CL. Besides, the relatively low limiting current density (around 100 A·m^{-2} in our work) makes the distinction between these two approximations vanished [49]. For simplicity, the Tafel equation thus is adopted to describe the HOR rate j (A·m^{-3}) [31],

$$j=\frac{i_{\mathrm{ref}}}{\Delta}\left(\frac{c_{\mathrm{Pt}}}{c_{\mathrm{ref}}}\right)^{0.5}\exp\left(\frac{\alpha F}{RT}\eta\right) \tag{14}$$

with i_{ref}, c_{ref}, and α denoted as the reference transfer current density, hydrogen concentration, and the transfer coefficient, respectively. Δ is a parameter that translates the reaction rate on a surface into a volume-based rate as addressed by Siddique and Liu [42]. The electrochemical kinetic c_{ref} and i_{ref} are chosen as 40 mol·m^{-3} and 1940 A·m^{-2}, respectively [31]. Δ is given as the inverse of the mesh resolution δx in the present work. c_{Pt} refers to the hydrogen concentration at Pt surfaces. The overpotential η is calculated as $\eta=\phi_{\mathrm{s}}-\phi_{\mathrm{ion}}-U$, where ϕ_{s} is assumed to be the applied voltage throughout the working electrode and U is the Nernst potential calculated as,

$$U=-\frac{RT}{2F}\log\frac{c_{\mathrm{H_2,we}}}{c_{\mathrm{H_2,re}}} \tag{15}$$

where the subscripts "we" and "re" refer to the working and reference electrodes, respectively. The hydrogen molar consumption rate j_{H2} (mol·m^{-3}·s^{-1}) is calculated as $j_{\mathrm{H2}}=-j/2F$. It should be noted that the chemical reaction parameters (such as η and i_{ref}) may affect the current density, but will not affect the diffusion-limited i_{lim}.

Due to the possible limited transfer rate of the reactant at the Pt/ionomer interfaces k_{ads}, the presence of the adsorption resistance R_{ads} is also hypothesized [20]. Therefore, the conjugated interfacial conditions can be expressed as,

$$-D_{\mathrm{ion}}\frac{\partial c_{\mathrm{ion}}}{\partial \mathbf{n}}=k_{\mathrm{ads}}\left(c_{\mathrm{ion}}-c_{\mathrm{Pt}}\right)=-j_{\mathrm{H_2}}\delta x \tag{16}$$

Correspondingly, interfacial conditions for the proton transport at the Pt/ionomer interfaces can be expressed as,

$$-\kappa\frac{\partial \phi_{\mathrm{ion}}}{\partial \mathbf{n}}=-j\delta x \tag{17}$$

Since the hydrogen concentration discontinuity exists at the interfaces of ionomer/pore and Pt/ionomer, special numerical treatments of Eqs. (12), (16) and (17) are needed and will be addressed in Section 2.1.2.

2.1.1 Multiple-relaxation-time lattice Boltzmann method

To describe the transport processes of hydrogen and proton in the CL at the mesoscopic level, LBM with the multiple-relaxation-time (MRT) collision operator is used due to its higher numerical stability [50]. The macroscopic transport phenomenon can be fully recovered by a collective behavior of the pseudo-particles with a set of distribution functions [51]. In the present study, the D3Q7 (7 discrete velocities in 3 dimensions) model is selected for its simplicity. The evolution of the populations can be expressed as follows,

$$f_\alpha\left(\mathbf{x}+\mathbf{e}_\alpha\delta t,t+\delta t\right)-f_\alpha\left(\mathbf{x},t\right)=-\mathbf{M}^{-1}\mathbf{\Lambda}\mathbf{M}\left(f_\alpha\left(\mathbf{x},t\right)-f_\alpha^{\mathrm{eq}}\left(\mathbf{x},t\right)\right) \tag{17}$$

where $f_\alpha(\mathbf{x}, t)$ is the distribution function at the lattice site $\mathbf{x}$ and time t in the αth direction. The lattice velocity $\mathbf{e}_\alpha$ and the weight coefficient ω_α are given as: $\mathbf{e}_0=[0, 0, 0]$, $\mathbf{e}_1=[c, 0, 0]$, $\mathbf{e}_2=[-c, 0, 0]$, $\mathbf{e}_3=[0, c, 0]$, $\mathbf{e}_4=[0, -c, 0]$, $\mathbf{e}_5=[0, 0, c]$, $\mathbf{e}_6=[0, 0, -c]$, $\omega_0=j_0$ and $\omega_{1\text{-}6}=(1-j_0)/6$ with the lattice sound speed $c=\delta x/\delta t$ and the parameter j_0 ranging from 0 to 1. The equilibrium distribution function $f_\beta^{\mathrm{eq}}\left(\mathbf{x},t\right)$ is given as $f_\beta^{\mathrm{eq}}\left(\mathbf{x},t\right)=\left(1+e_{\beta j}u_j/c\varepsilon_D\right)\omega_\beta\varphi$ with φ and ε_D calculated as $\varphi=\sum_{\alpha=0}^{6}f_\alpha\left(\mathbf{x},t\right)$ and $\varepsilon_D=(1-j_0)/3$, respectively. Details on the transformation matrix $\mathbf{M}$ and its corresponding diagonal matrix $\mathbf{\Lambda}$ can be found in SI. The relaxation coefficients τ_{ij} satisfying the constraint $0\leq 1/\tau_{ij}<2$ are related with the diffusion coefficient tensor D_{ij} as,

$$\tau_{ij} = \frac{1}{2}\delta_{ij} + \frac{1}{c\varepsilon_D \delta x} D_{ij} \tag{18}$$

In the present work, the isotropic diffusion has been considered and the following equation on the relationship of the relaxation coefficients are applied,

$$\tau_0 = 1, \quad \tau_4 = \tau_5 = \tau_6 = \frac{1}{2} + \frac{1}{6\left(\tau_{11,22,33} - 1/2\right)} \tag{19}$$

The numerical implementation of Eq. (17) is usually divided into a collision step and a streaming step,

$$\hat{f}_\alpha(\mathbf{x},t) = f_\alpha(\mathbf{x},t) - \mathbf{M}^{-1}\mathbf{\Lambda}\left(m_\alpha(\mathbf{x},t) - m_\alpha^{\mathrm{eq}}(\mathbf{x},t)\right) \tag{20a}$$

$$f_\alpha(\mathbf{x} + \mathbf{e}_\alpha \delta t, t + \delta t) = \hat{f}_\alpha(\mathbf{x},t) \tag{20b}$$

where $\hat{f}_\alpha$ is the post-collision population. With the Chapman-Enskog expansion technology, the following standard governing equation without a source term can be obtained,

$$\frac{\partial \varphi}{\partial t} + \frac{\partial}{\partial x_i}(u_i \varphi) = \frac{\partial}{\partial x_i}\left(D_{ij}\frac{\partial \varphi}{\partial x_j}\right) \tag{21}$$

where the velocity components u_i equal 0 in the present work.

For the hydrogen diffusion process, D_{ij} is the hydrogen diffusivity. Specifically, the local diffusivity of hydrogen is given as $D_{\mathrm{H2:mix}}$ for the nodes representing pores based on the pore size distribution and specified as D_{ion} for the nodes representing ionomer. The values of $D_{\mathrm{H2:mix}}$ and D_{ion} usually differ by 5 or 6 orders of magnitude, which result in big difference of the relaxation coefficients for different phases. Validation on the robustness of the present MRT model with the relaxation coefficient ranging from 0.5005 to 100000 thus has been provided in SI. In our simulation, the maximum relaxation coefficient of the pores, which corresponds to the largest pore size, is 10000.

For the proton transport process, D_{ij} is given as the proton conductivity κ. As the value of κ is typically several orders of magnitude higher than $D_{\mathrm{H2:mix}}$, the following treatments on the proton transport equation are performed to avoid the possible numerical instability caused by the incredible high relaxation coefficient:

The local proton potential ϕ_{ion} described in Eq. (4a) can be obtained from the following equation by introducing an artificial diffusivity, D_0, with its value of the same order-of-magnitude of $D_{\mathrm{H2:mix}}$,

$$\nabla\cdot\left(D_0\nabla\phi_{\mathrm{ion}}\right)=-D_0 j/\kappa \tag{22}$$

Correspondingly, the relaxation coefficient for the proton transport in ionomer phases is given as,

$$\tau_{\mathrm{ion}}=\frac{2D_0}{1-j_0}\frac{dt}{dx^2}+0.5 \tag{23}$$

With the above strategy, the numerical robustness of the method considering the coupling between the proton and hydrogen transport processes can be guaranteed.

2.1.2 Conjugated interfacial condition treatments

Based on our previous work [52], the interface can be regarded as a shared boundary by different domains. For different macroscopic interfacial conditions, the corresponding unknown populations can be converted with the expressions for a half-lattice interface shown in Fig. 2(a). The whole domain is divided into two sub-domains, Ω_{A} and Ω_{B}, with different transport properties separated by an interface Γ. Φ_n is the normal flux on the boundary pointing inward to the domain. In this section, we mainly focus on the numerical treatments of the unknown populations at the interfaces of ionomer/pore and Pt/ionomer. In the following analyses, the respective populations of hydrogen and proton are denoted as f and g.

Fig. 2 Schematic description of the lattice nodes and its numerical treatment, (a) treatment of the conjugated mass transfer between the pore and ionomer; (b) treatment of the chemical reaction at the platinum surfaces

As shown in Fig. 2(a), the unknown populations at the interfaces of ionomer and pore are obtained with a combination of the known post-collision populations and the interfacial boundary values,

$$f_i\left(\mathbf{x}_{\mathrm{A}},t+\delta t\right)=-\hat{f}_{\bar{i}}\left(\mathbf{x}_{\mathrm{A}},t\right)+\varepsilon_D c_{\mathrm{A}} \tag{24a}$$

$$f_{\bar{i}}\left(\mathbf{x}_{\mathrm{B}},t+\delta t\right)=-\hat{f}_{i}\left(\mathbf{x}_{\mathrm{B}},t\right)+\varepsilon_{D}c_{\mathrm{B}} \tag{24b}$$

where $\mathbf{x}_{\mathrm{A}}$ is the first nearest interior lattice nodes along $\mathbf{e}_i$ direction in domain A. Similarly, $\mathbf{x}_{\mathrm{B}}$ is the first nearest interior lattice nodes along $\mathbf{e}_{\bar{i}}$ direction in domain B. $f_i\left(\mathbf{x}_{\mathrm{A}},t+\delta t\right)$ and $f_{\bar{i}}\left(\mathbf{x}_{\mathrm{B}},t+\delta t\right)$ are the respective unknown populations in the components of pore and ionomer. $\hat{f}_{\bar{i}}\left(\mathbf{x}_{\mathrm{A}},t\right)$ and $\hat{f}_{i}\left(\mathbf{x}_{\mathrm{B}},t\right)$ are the post-collision populations of pore and ionomer, respectively, and c_{A} and c_{B} are the respective interfacial values in domains A and B, respectively. Meanwhile, the unknown populations can also be calculated with a combination of the same post-collision populations and the interfacial fluxes,

$$f_{i}\left(\mathbf{x}_{\mathrm{A}},t+\delta t\right)=\hat{f}_{\bar{i}}\left(\mathbf{x}_{\mathrm{A}},t\right)+\left(\delta t/\delta x\right)\varPhi_{i,\mathrm{A}} \tag{25a}$$

$$f_{\bar{i}}\left(\mathbf{x}_{\mathrm{B}},t+\delta t\right)=\hat{f}_{i}\left(\mathbf{x}_{\mathrm{B}},t\right)+\left(\delta t/\delta x\right)\varPhi_{\bar{i},\mathrm{B}} \tag{25b}$$

where $\varPhi_{i,\mathrm{A}}$ and $\varPhi_{\bar{i},\mathrm{B}}$ are the respective interfacial fluxes in domains A and B, respectively.

Combining Eqs. (12), (24), and (25), the unknown interfacial populations at the ionomer/pore surfaces can be obtained,

$$f_{i}\left(\mathbf{x}_{\mathrm{A}},t+\delta t\right)=\frac{\left(\varepsilon_{D}/k_{\mathrm{dis}}\,\delta x/\delta t+1/K-1\right)\hat{f}_{\bar{i}}\left(\mathbf{x}_{\mathrm{A}},t\right)-2\hat{f}_{i}\left(\mathbf{x}_{\mathrm{B}},t\right)}{\varepsilon_{D}/k_{\mathrm{dis}}\,\delta x/\delta t-1/K-1} \tag{26a}$$

$$f_{\bar{i}}\left(\mathbf{x}_{\mathrm{B}},t+\delta t\right)=\frac{\left(\varepsilon_{D}/k_{\mathrm{dis}}-1/K+1\right)\hat{f}_{i}\left(\mathbf{x}_{\mathrm{B}},t\right)-2/K\,\hat{f}_{\bar{i}}\left(\mathbf{x}_{\mathrm{A}},t\right)}{\varepsilon_{D}/k_{\mathrm{dis}}\,\delta x/\delta t-1/K-1} \tag{26b}$$

with the partition coefficient $K=H/RT$.

As shown in Fig. 2(b), attention now is turned to the treatment of the source terms for the hydrogen and proton transport processes at the Pt/ionomer surfaces due to the chemical reaction. The following equations can be obtained,

$$g_{\bar{i}}\left(\mathbf{x}_{\mathrm{B}},t+\delta t\right)=-\hat{g}_{i}\left(\mathbf{x}_{\mathrm{B}},t\right)+\varepsilon_{D}\phi_{\mathrm{ion}} \tag{27a}$$

$$g_{\bar{i}}\left(\mathbf{x}_{\mathrm{B}},t+\delta t\right)=\hat{g}_{i}\left(\mathbf{x}_{\mathrm{B}},t\right)+\delta t/\delta x\,\varPhi_{\mathrm{ion}} \tag{27b}$$

$$f_{\bar{i}}\left(\mathbf{x}_{\mathrm{B}},t+\delta t\right)=-\hat{f}_{i}\left(\mathbf{x}_{\mathrm{B}},t\right)+\varepsilon_{D}c_{\mathrm{ion}} \tag{27c}$$

$$f_{\bar{i}}\left(\mathbf{x}_{\mathrm{B}},t+\delta t\right)=\hat{f}_{i}\left(\mathbf{x}_{\mathrm{B}},t\right)+\delta t/\delta x\,\varPhi_{\mathrm{H_2}} \tag{27d}$$

$$\varPhi_{\mathrm{H_2}}=-k_{\mathrm{ads}}\left(c_{\mathrm{ion}}-c_{\mathrm{Pt}}\right)=j_{\mathrm{H_2}}\delta x=-\kappa/D_0\,\varPhi_{\mathrm{ion}}/2F \tag{27e}$$

where $g_{\bar{i}}\left(\mathbf{x}_{\mathrm{B}},t+\delta t\right)$ and Φ_{ion} refer to the unknown interfacial population of the proton potential and the interfacial flux at the Pt/ionomer surfaces, respectively. Therefore, the unknown parameters: $g_{\bar{i}}\left(\mathbf{x}_{\mathrm{B}},t+\delta t\right)$, $f_{\bar{i}}\left(\mathbf{x}_{\mathrm{B}},t+\delta t\right)$, ϕ_{ion}, c_{ion}, Φ_{ion}, Φ_{H2}, and c_{Pt}, can be analytically solved. Numerical validations on the above interfacial treatments of the present methodology are provided in SI. Besides, the mesh independent test is also performed as given in SI.

2.2 Catalyst-layer reconstruction

The transport processes and performance of the CL are highly affected by its morphology, which depends on both composition and processing. Typically, the imaging combination techniques such as X-ray computed tomography or FIB-SEM and the stochastic generation methods are always adopted for the CL reconstruction. Cetinbas et al. [37] incorporated data from nano-CT, ultra-small angle X-ray scattering, TEM and porosimetry to reconstruct the 3-D microstructures. Due to its merits such as the low cost and easy implementation, several stochastic generation methods have been developed including the Gaussian random field method [53], the sphere-based annealing method [54] and the random carbon sphere method [38]. Recently, Sabharwal et al. [55] reconstructed the CL with two components (pore and solid) based on a random overlapping sphere algorithm and applied several statistical correlation functions to characterize the CL. Chen et al. [41] and Ishikawa et al. [56] reconstructed the 3-D structure of the CL by mimicking the actual Pt particles, carbon aggregates and ionomer. Malek et al. [57] applied a coarse-grained molecular dynamics methodology to explore the microstructure formation process in the CL.

Inspired by the fabrication process of the CL, the whole reconstruction processes in the present work can be divided into three steps. First, the primary carbon particles are dispersed. The carbon particle size distribution is based on the experimental data [58]. The location and size of the first particle are randomly determined in the domain. To ensure the carbon particles are connected, two rules are made before putting a new particle: the volume-overlapping ratio of the new particle with its neighbor particles should be in the range of 0 and 0.1, and the total overlapping number of the particles should be lower than 8 to avoid agglomeration. Since the diameter of the newly placed particle may be different from the existing ones, we have calculated all the possible volume-overlapping ratios. Only when the two rules are satisfied will the new particle be inserted. The overlapping treatment of the particle spheres in our model is quite different from that of Sabharwal et al. [55]. As the particle size in their model is the same, the overlapping is only controlled with a penetration parameter and starts as the number of particles is sufficiently large. The carbon dispersion will not be terminated until the volume fraction of carbon equals $\varepsilon_C+\alpha_1\varepsilon_{Pt}$. The parameter α_1 is within 0 and 1.

Second, ionomers are coated on the carbon particles. Loop over all the primary particles, the carbon particles will be added one layer of ionomer if the randomly generated number is lower than a given small probability c_d. Obviously, the coated ionomer thickness on carbon particles will become more uniform if c_d is relatively lower. Repeat this step until the volume fraction of ionomer equals ε_{ion}+ (1-α_1) ε_{Pt}.. The ionomer thicknesses for all the particles can be obtained by recording the number of layers. Therefore, the ionomer thickness distribution can be acquired with the thickness of one layer equaling the mesh resolution. For the last step, if the CL is diluted with bare carbons with its volume fraction of ε_{bare}, the carbon particles are assumed to be inactive if a randomly given number is smaller than ε_{bare}. Pt particles are assigned at the interfaces of carbon particles and ionomer films. The nodes representing the interfaces of the active carbon particles and ionomer films are labelled. If a randomly given number is smaller than α_1, the nodes representing carbon will change to Pt. Otherwise, the nodes representing ionomer will change to Pt. In the present work, we choose α_1=0.1 and c_d=10^{-7}. Actually, the parameter α_1 can be used to tune the roughness factor f_{Pt}, and smaller α_1 will result in relatively higher f_{Pt}.

The volume fractions of different components in the CL are calculated based on the characteristic parameters of the CL during its fabrication process,

$$\varepsilon_{\mathrm{Pt}} = \frac{L_{\mathrm{Pt}}}{l\rho_{\mathrm{Pt}}} \tag{28a}$$

$$\varepsilon_{\mathrm{C}} = \left(1-\varepsilon-\varepsilon_{\mathrm{Pt}}\right) \Big/ \left(1+\frac{\rho_{\mathrm{C}}}{\rho_{\mathrm{ion}}}\gamma\right) \tag{28b}$$

$$\varepsilon_{\mathrm{ion}} = 1-\varepsilon-\varepsilon_{\mathrm{C}}-\varepsilon_{\mathrm{Pt}} \tag{28c}$$

where γ is the ratio of ionomer and carbon by mass, l is the thickness of CL, and ε is the porosity. Densities of carbon, platinum, and ionomer are set as 1.8, 21.45, and 2 g·cm^{-3}, respectively [41].

To validate the reliability of the present reconstruction method, the structural parameters of the CL adopted in Cetinbas et al. [37] has been chosen. Detailed structural parameters are: γ = 0.8, ε = 0.42, l =3.75 μm, L_{Pt}=0.092 mg·cm^{-2}, ω=30%. ω is the ratio of Pt and carbon by mass. Note that the de-alloyed Pt-Ni other than the pure Pt were supported on the carbon black in their experiment. Therefore, a part of Pt particles based on the given mass fraction of Ni (43%) is changed to Ni after the reconstruction process. As shown in Fig. 3(a), the computational domain is 1×1×1μm with the same mesh resolution of 2.5 nm as Cetinbas et al.[58]. It can be found that the primary carbon particles with different sizes are coated with the ionomer with different thicknesses, and the Pt particles are dispersed on the surfaces of carbon particles. Fig. 3(b) presents the normalized volume fractions of different components along the thickness direction. All the components are relatively uniform with the normalized volume fractions ranging from 0.85 to 1.2. Fig. 3(c) presents the comparisons of the carbon particle number and ionomer thin-film volume fractions between the USAXS data [59] and the reconstructed data. The predicted data matches well with the experiments. The carbon particle diameter ranges from 20 to 70 nm with the majority of the carbon particle size of 45 nm. The ionomer thin-film thickness ranges from 2.5 to 25 nm and the majority of the thin-film thickness is around 10 nm. Only a small portion of the thicknesses is higher than 25 nm. Obviously, the unevenness of the particle sizes and the thin-film thicknesses makes the existing analytical models accurately predicting the transport resistances in the CL difficult.

Pore size distribution (PSD) is essential for the hydrogen transport in pores of the microstructure. In this paper, the local pore diameter for a given pore node is computed by taking an average of 13 different lengths proposed by Djilali's group [38]. Details are as follows: for each pore node, a pore length is computed by moving in a given direction both backward and forward through the computational domain until a non-pore node is reached and a "length" of the pore node in a given direction can be computed. Thirteen different directions are used to compute the average pore diameter. Fig. 3(d) presents the comparison of the statistically obtained PSD between the present work and Cetinbas et al.[58] (the pore sizes are grouped every 20 nm). Note that the inserted figure in Fig. 3(d) is the real PSD. The shape of the present PSD matches well with Lange et al. [38] and Chen et al. [41] who also used the same method to obtain the PSD. As the mesh resolution is 2.5 nm, the pore diameter smaller than 2.5 nm cannot be distinguished. The pore sizes range from 2.5 to 350 nm, covering the primary and secondary pores. With the mercury intrusion porosimetry testing, the pore size of the CL given by Yu and Carter [60] ranges from 0 to 300 nm, and that measured by Ihonen et al. [61] and Ozden et al. [62] ranges from 2nm to several microns. However, in the measurements given by Soboleva et al. [63], the pore size ranges from 3 to 110 nm. The significant distinction of the PSD may be attributed to the difference in the structural parameters. Yu and Carter [60] found that the mean pore size decreases greatly with γ and lower porosity leads to small mean pore size. Sabharwal et al.[40] concluded that the mean pore size increases with the particle size. Compared our results with those of Cetinbas et al. [58], high accordance of the pore volume fractions and the mean pore size can be observed. The mean pore size we predicted is around 160 nm, which is close to 180 nm given by Cetinbas et al. [58]. This indicates that our reconstructed model can capture the details of the CL morphology. It is worth noting that the present mean pore size is comparatively higher than those reconstructed by Lange et al. [64] and Sabharwal et al. [55]. Apart from the structural parameters adopted in different studies, the reconstructed domain size and the PSD calculation method may account for the difference. In the work of Lange et al. [64], the domain size is 200×200×200 nm, and that in the work of Sabharwal et al. [40] is 600×600×600 nm. A smaller domain size will surely result in smaller pore size distribution. Although the domain size in Fig. 3(a) is 1000×1000×1000 nm, periodic boundary conditions are adopted when calculating the PSD. Therefore, the pore size obtained with our method is comparatively larger.

Fig. 3 Comparisons of the numerical reconstructed CL with the existing data [58], (a) morphology of the reconstructed CL (pore: white, carbon: black, platinum: red, ionomer: cyan); (b) normalized volume fractions of all the components of the CL along the thickness direction; (c) primary particle size number and ionomer thin-film thickness distributions; (d) pore size distribution. The structural parameters of the CL are $\gamma = 0.8$, $\varepsilon = 0.42$, $l = 3.75\ \mu m$,

L_{Pt} =0.092 mg·cm^{-2}, ω=30%.

Roughness factor f_{Pt} is a critical parameter to characterize $R_{\mathrm{H_2}}^{\mathrm{Pt}}$ accurately. Since all of the Pt particles are attached on carbon particles during the reconstruction process, the Pt surface with its neighboring nodes labeled as ionomer may serve as the electrochemical surface area since carbon particles provide transport pathways for electrons and ionomers provide transport pathways for proton and hydrogen. Obviously, the above treatment will overestimate the electrochemical surface area since isolated ionomers coated on the carbon particles are not excluded. To overcome this issue, the proton transport process without considering the chemical reaction in the CL microstructure is first conducted. A randomly chosen positive value of the ionic potential is specified at the CL/MEM interface, and no flux boundary condition is given at the CL/GDL interface. If the simulation reaches steady state, the potential of the connected ionomer should be the same as the chosen one. Therefore, the interfacial surfaces area of the Pt and ionomer with the potential of the ionomer lower than the chosen value will be excluded. In this way, one can guarantee f_{Pt} is the effective electrode surface area. The Pt-mass-specific electrochemical surface area a_{ECSA} can be obtained by normalizing the effective electrochemical surface area by the Pt mass in the CL. Table 1 presents the comparison of a_{ECSA} between the predicted data and the existing experimental data [8, 28, 37]. Details on the structural parameters of the CL for the experimental data are also provided. It can be found that the values of a_{ECSA} predicted with the reconstructed structures match quite well with all the experimental data with the maximum deviation of 5.7%. In addition, the numerically predicted a_{ECSA} for the structural parameters of the CL adopted in [28] is also close to 73.9 m^{2}·g$^{-1}_{\mathrm{Pt}}$ that measured by Suzuki et al. [20] and 70.0 m^{2}·g$^{-1}_{\mathrm{Pt}}$ measured by Jomori et al. [65]. Therefore, it is convincible to use the present reconstructed CL to predict $R_{\mathrm{H_2}}^{\mathrm{Pt}}$.

Table 1. Comparison of the Pt-mass-specific electrochemical surface area a_{ECSA} between the predicted data and the existing experimental data [8, 28, 37]

2.3 Boundary conditions and solution strategy

As the CL thickness may vary with L_{Pt}, only the size of the CL cross-section 300×300 nm along the thickness direction is assigned with the mesh resolution of 2.5 nm. Periodic conditions are specified in the other two directions. For the first step that the hydrogen transport process in pores is not considered, the hydrogen concentration throughout the CL pores remains to be $c_{\mathrm{H2,bulk}}$ according to the experimental working conditions mentioned above. For the second step that the hydrogen transport process in pores is considered. As the transport resistance of the CH and GDL exists, the hydrogen concentration at the interface of CL and gas diffusion layer is corrected iteratively,

$$c_{\mathrm{CL/GDL}} = c_{\mathrm{H_2,bulk}} - \left(R_{\mathrm{GDL}} + R_{\mathrm{CH}}\right) i/2F \quad \text{and} \quad R_{\mathrm{CL}} = 2Fc_{\mathrm{CL/GDL}}/i \tag{29}$$

In our model, we corrected the hydrogen concentration at the interface of CL and GDL every 2000 time steps to avoid the numerical instability due to a frequently variation of the boundary conditions. The current density i can be calculated simply by integrating the chemical reaction rate j at the reaction surfaces and then normalized by the cross-section area A, i.e., $i = \sum j\left(\delta x\right)^3 / A$. No-flux boundary condition of hydrogen is defined at CL/MEM interface. The conjugated hydrogen transport at the ionomer/pore interfaces and ionomer/Pt interfaces is automatically implemented with Eqs. (26) and (27). For the transport process of proton, no-flux boundary condition of proton is specified at CL/GDL interface, and a zero ionic potential is specified at the CL/MEM interface. Half-lattice method is adopted to treat the boundary conditions and the conjugated interfaces. For the maximum computational size we adopted is 9300×300×300 nm, the mesh numbers along different directions are 3750×120×120 (53.76 million). It takes about 12 hours for one case with 160 CPU cores to reach steady state. If only the first step is simulated, the CPU time can be greatly reduced to 2 hours.

3. Results and discussion

3.1 Characterization of the transport processes in the CL

The limiting current density can be obtained either by changing the electronic potential ϕ_s or the reference current density i_{ref} in Eq. (14). Since we mainly focus on the limiting current, the dependence of the polarization behaviors on the above parameters is not of prime consideration (see Fig. S5 in SI). As shown in Fig. S5, the current density increases with the reference current density and then reaches a plateau. Similarly, one can also obtain the proton potential dependent current density. Note that the limiting current density is only related with R_{CL}, it will not be affected by the chemical reaction parameters such as the reference current density, overpotenial, and reference hydrogen concentration.

Fig. 4 presents the comparison of the numerical data and the experimental data [28] at different L_{Pt} with the detailed structural parameters of γ = 0.75, ε = 0.55, and ω=18.3%. Detailed structural parameters of the simulated cases are given in Table S1. The numerical simulated L_{Pt} are 0.03, 0.05, 0.08 and 0.10 mg·cm^{-2}, with the respective thicknesses are 2.80, 4.68, 7.5 and 9.30 μm. The hydrogen permeation coefficient ψ_{H2} in the ionomer thin-film is assumed to be 5.9% of the bulk, and the interfacial transport resistances are all neglected. Considering the computational cost, the maximum thickness of the CL is chosen as 9.3 μm, corresponding to L_{Pt} of 0.10 mg·cm^{-2} with the total meshes of 53.76 million. It can be found that all the numerically predicted data agree well with the experimental data [28]. As expected, R_{CL} increases significantly with the reduction of L_{Pt}, and R_{CL} shows linear trend with the inverse of f_{Pt}. The slope of the curve is the local transport resistance $R_{H_2}^{Pt}$, with the predicted value (1867 s·m^{-1}) matching well with the experimental result (1863 s·m^{-1}) [28].

Fig. 4 Comparison of the transport resistance R_{CL} between numerical data and the experimental data [28] versus platinum loadings L_{Pt} and roughness factors f_{Pt}

As addressed before, the accuracy of the predicted $R_{H_2}^{Pt}$ may be affected by the linear fitting method for constant carbon dilution. We have compared the values of $R_{H_2}^{Pt}$ for four different L_{Pt} with the first step introduced in section 2.3. The predicted values are 1854, 1889, 1889 and 1905 s·m^{-1}, respectively. The average value is 1885 s·m^{-1} and the standard deviation of errors is 18.6 s·m^{-1}. Compared with the average value, the maximum deviation of $R_{H_2}^{Pt}$ for the four different cases is 1.16%. Discrepancy between the average value and the linear fitted one are within 1.00%, confirming the reliability of $R_{H_2}^{Pt}$ calculated with the first step. Such a small difference may result from small R_{Pore} for different L_{Pt}. Besides, despite of the stochastic reconstruction method we adopted, almost the same values of $R_{H_2}^{Pt}$ are obtained for different reconstructed CL with the same input structural parameters. Therefore, only single case for one set of the microstructural parameters is adopted in the following study by considering the computational cost.

For better understanding the transport processes in the CL, Fig. 5(a) illustrates the contours of the hydrogen concentrations, overpotential and chemical reaction rate at the cross-section of y=150 nm with L_{Pt} of 0.05 mg·cm^{-2}. The hydrogen concentration in pores c_p is relatively uniform as the limiting current density i_{lim} is comparatively small (83.4 A·m^{-2}). Therefore, i_{lim} is expected to exhibit a linear trend with f_{Pt} approximately (assuming that coverage over the Pt sites remains above a critical value for percolation). The hydrogen concentration in ionomers c_{ion} changes greatly since the thicknesses of the thin-film coated on the carbon particles vary greatly. The value of c_{ion} is comparatively smaller than that of c_p as the partition coefficient K equals 1.72. The overpotential η is relatively uniform throughout the ionomer. As the chemical reaction only occurs at the Pt-ionomer-carbon surfaces, the chemical reaction rate in the CL is discrete. Fig. 5(b) presents the face-averaged value of c_p, c_{ion}, η and j along the thickness direction. c_p decreases along the thickness due to the chemical reaction. Unlike c_p, c_{ion} fluctuates due to the ionomer morphology. η increases along the thickness as the ionic potential decreases along the thickness. However, the potential drop is also comparatively small due to low current density i_{lim} and high proton conductivity κ. j shows a similar trend with c_{ion} as it is directly related with c_{ion} at the reaction sites. This also indicates that the chemical reaction rate is dependent on the ionomer morphology, and which does not show the same trend with c_p as widely adopted in the analytical results [8] (see Eqs. (2) and (3)). This will be addressed to evaluate R_{Pore} in Section 3.3.

Fig. 5 Illustrations of the hydrogen concentration and chemical reaction rate in the catalyst *layer at the cross-section of y=150 nm. (a) contours of c_p in pore, c_{ion} in ionomer, η in ionomer and chemical reaction rate j at platinum surfaces; (b) variations of c_p, c_{ion}, η and j along the thickness direction. The structural parameters are: γ=0.75, ε=0.55, l=4.68 μm, L_{Pt}=0.05mg·cm^{-2}, and ω=18.3%.*

In the above analyses, we assume the ionomer thin-film is more resistive and $R_{\mathrm{H_2}}^{\mathrm{Pt}}$ is purely attributed to R_{I}. If the permeation coefficient of the bulk ψ_0 is adopted, the simulated local transport resistance (110 s·m^{-1}) is one order-of-magnitude lower than the existing experimental data [26-28, 34]. Apart from the possible reduction of the transport properties of the ionomer thin-film compared with the bulk, some unknown factors including the existence of the interfacial transport resistances due to the dissolution and adsorption may also account for the observed high $R_{\mathrm{H_2}}^{\mathrm{Pt}}$. Detailed parameter sensitivities of them on $R_{\mathrm{H_2}}^{\mathrm{Pt}}$ are thus needed. In the following section, we first performed the parameter sensitivity analyses for one particular microstructural parameters (γ=0.75, ε=0.55, ω=18.3%, L_{Pt} = 0.08 mg·cm^{-2}, and l=7.50 μm), and then validated the input model parameters with the existing experimental data for different γ. In this way, a set of the suitable input model parameters can be acquired.

3.2 Parameter sensitivity of local transport resistance

As the geneses of the dissolution and adsorption resistances are quite different, parameter sensitivity analyses are performed separately. Experimental and analytical quantifications of each interfacial resistance are sparse as they are coupled and undoubtedly affect each other [5, 10]. The total interfacial transport resistance measured by Suzuki et al. [36] and Kudo et al. [18] ranges from 1000 to 10000 s·m^{-1}. Molecular dynamics simulation performed by Jinnochi et al. [10] shows that R_{ads} was two orders of magnitude higher than R_{dis}. In the present work, the minimum value we adopted for the interfacial reaction rates is around 0.0002 m·s^{-1}. As seen in Fig. 6, the x-axis refers to the ratio of the permeation coefficient between the numerical adopted value and the bulk one $\psi_0\psi_{\mathrm{H_2}}^{-1}$, and the y-axis on the top and bottom of the figure refers to k_{dis}^{-1} and k_{ads}^{-1}, respectively. The structural parameters of the CL are given in

Table S2. The newly proposed method to calculate $R_{H_2}^{Pt}$ is adopted in this section. The best fitting curves mean the predicted $R_{H_2}^{Pt}$ is the same as the experimental data [28].

Attention is first turned to the effect of $\psi_0\psi_{H_2}^{-1}$ on $R_{H_2}^{Pt}$. For any specific interfacial resistances, it can be found that $R_{H_2}^{Pt}$ increases with the decrease of ψ_{H2} as R_I is related with ψ_{H2} and the thin-film thickness directly. The distance between two contour lines of $R_{H_2}^{Pt}$ is almost the same, indicating $R_{H_2}^{Pt}$ increases linearly with $\psi_0\psi_{H_2}^{-1}$. This phenomenon is analogous to the validation case in SI by replacing the term K/D_2 with K/D_{ion}, which can be further simplified as RT/ψ_{H2}. This also agrees with the existing literature which assume the one-dimensional transport of the reactant in the CL [28, 34, 66]. If both of the interfacial resistances are neglected, the best fitting value of ψ_{H2} would be 5.9% of the bulk (see Case 5 in Fig. 6). Detailed input model parameters of the cases in Fig. 6 are listed in Table S2.

The influence of the dissolution reaction rate k_{dis} and the permeation coefficient ψ_{H2} on $R_{H_2}^{Pt}$ is provided on the top of Fig. 6. The value of k_{ads}^{-1} is set as 0 and the value of k_{dis}^{-1} ranges from 0 to 5600 $s\cdot m^{-1}$. By changing the value of $\psi_0\psi_{H_2}^{-1}$ from 1 to 20, the limiting current density for different input parameters can be acquired. Correspondingly, the total transport resistance of R_{CL} for the first step of the newly proposed method is obtained. The value of $R_{H_2}^{Pt}$ can be simply obtained with $R_{H_2}^{Pt}=R_{CL}f_{Pt}$. As expected, $R_{H_2}^{Pt}$ increases with k_{dis}^{-1}. The value of k_{dis}^{-1} is comparatively higher than $R_{H_2}^{Pt}$ if the bulk permeation coefficient is adopted (see Case 1 in Fig. 6). Despite of the analogous transport process of the reactant from pore to ionomer and from ionomer to Pt surface, the ionomer roughness factor f_{ion}, defined as the interfacial surface area between the pore and ionomer normalized by the cross-section of the CL, is quite different from f_{Pt}. The ratio of f_{ion} relative to f_{Pt} is 5.75 for the present case. Therefore, the contribution of k_{dis}^{-1} to $R_{H_2}^{Pt}$ is highly weakened. A rough and idealized estimation of the contribution of k_{dis}^{-1} to $R_{H_2}^{Pt}$ is given as [34],

$$R_{dis} = k_{dis}^{-1} f_{Pt} / \left(f_{ion} + f_{Pt} \right) \tag{30}$$

By substituting the data in Case 1 to Eq. (30), the calculated R_{dis} is 793 s·m^{-1}. The sum of R_{dis} and R_{I} (110 s·m^{-1}) is far lower than the numerical estimated data (1889 s·m^{-1}). Inspired by the analytical equation we provided in the validation case, the partition coefficient K should be taken into account to estimate the total transport resistance. Multiply K by R_{dis} calculated with Eq. (30), the newly obtained R_{dis} is 1364 s·m^{-1}. The sum of R_{dis} and R_{I} is 1474 s·m^{-1}, which is still lower than the numerical estimated data with the deviation around 21%. This indicates that the analytical result without considering the real microstructure of the CL underestimates R_{dis} greatly. In fact, the analytic model assumes the particle carbon sizes and the ionomer thicknesses are uniformly distributed and all the surface areas of ionomer and pore are available for the reactant transport in the CL, which are quite different from the real morphology of the CL. Besides, the surface area available for dissolution is highly dependent on the ionomer morphology. The distributions of Pt/C ratio ω of the particles may also vary greatly. As seen in Fig. S6 in SI, the effective surface area of the ionomer coated on the particles are quite different for different ω. Moreover, the effective surface area also differs for different R_{I}. As seen in Table 2, the contribution of k_{dis}^{-1} to $R_{\mathrm{H_2}}^{\mathrm{Pt}}$ increases with $\psi_0 \psi_{\mathrm{H_2}}^{-1}$. This is understandable as the diffusion distance from the outer spherical surface of the ionomer thin-film to the reaction surface differs. It is preferable for the hydrogen to transport from the surface area facing the reaction surface. Hence, the local R_{I} around the outer spherical surface varies greatly with the increase of $\psi_0 \psi_{\mathrm{H_2}}^{-1}$. The effective surface area for reactant flux from pore to ionomer decreases with R_{I}, resulting in the decreasing effective f_{ion}. This indicates that R_{dis} and R_{I} are highly coupled. Therefore, a thorough consideration of the structural parameters of the CL may improve the accuracy of the estimation of R_{dis}.

The influence of the adsorption reaction rate k_{ads} and the permeation coefficient ψ_{H2} on $R_{\mathrm{H_2}}^{\mathrm{Pt}}$ is provided on the bottom of Fig. 6. The value of k_{dis}^{-1} is set as 0 and the value of k_{ads}^{-1} ranges from 0 to 1100 s·m^{-1}. By changing the value of $\psi_0 \psi_{\mathrm{H_2}}^{-1}$ from 1 to 20, the value of $R_{\mathrm{H_2}}^{\mathrm{Pt}}$ for different input parameters can be obtained. Similar trend as k_{dis} can be observed. However, as the surface area of the reactant flux from ionomers to Pt cites is taken to be f_{Pt}, the value of k_{ads} is comparatively higher than k_{dis} for the same $R_{\mathrm{H_2}}^{\mathrm{Pt}}$. For example, in Case 1 and 3, the values of k_{ads}^{-1} and k_{dis}^{-1} are 985 and 5350 s·m^{-1}, respectively. The adsorption resistance R_{ads} related with k_{ads} can be expressed as [34],

$$R_{\mathrm{ads}} = Kk_{\mathrm{ads}}^{-1} \tag{31}$$

By substituting the data in Case 3 to Eq. (31), the sum of R_{ads} and R_{I} (110 s·m^{-1}) is 1804 s·m^{-1}, which is a little bit lower than the numerical estimated data. The reason may be explained as follow. As can be seen in Fig. S6 in SI, with the increase of R_{I}, the lateral reaction surfaces of Pt particles may become less active since the diffusion length of the reactant is longer, resulting in higher contribution of k_{ads}^{-1}. Besides, the reaction rate also influences the transport resistance as expressed in Eq. (S6), which is not included in Eq. (31). The contribution of k_{ads}^{-1} to $R_{\mathrm{H_2}}^{\mathrm{Pt}}$ is also presented in Table 2, which increases with $\psi_0\psi_{\mathrm{H_2}}^{-1}$. This indicates that R_{ads} and R_{I} are also coupled, and R_{ads} is dependent on the structural parameters of the CL.

Fig. 6 Parameter sensitivity analyses of the hydrogen permeation coefficient, dissolution reaction rate and adsorption reaction rate on the local transport resistance $R_{\mathrm{H_2}}^{\mathrm{Pt}}$

Table 2. Contribution of the interfacial reaction rates to the local transport resistance $R_{\mathrm{H_2}}^{\mathrm{Pt}}$

From the above analyses, both of the best fitting curves in Fig. (6) can give a reasonable value of $R_{\mathrm{H_2}}^{\mathrm{Pt}}$ for a specific structural parameters of the CL ($\gamma = 0.75$, $\varepsilon = 0.55$, and ω=18.3%). However, the corresponding parameters, representing different geneses of $R_{\mathrm{H_2}}^{\mathrm{Pt}}$, vary greatly. Further investigations on the determination of these parameters are highly needed. For simplicity, five cases are adopted to compare with the experimental data [28] for different I/C ratios γ. Fig. 7 presents the comparison of the numerically predicted and the experimental data [28] as a function of γ. Adding more ionomer leads to thicker thin-film coated on the Pt/C particles, resulting in more surface area for dissolution and hence higher a_{ECSA}. As shown in this figure, the numerically predicted a_{ECSA} increases slightly with γ when γ is higher than 0.6. However, it drops greatly with the reduction of γ since more Pt/C particles become uncoated and more ionomers become isolated. Fig. 8 shows the detailed information of the CL morphology for different γ. It can be found that the uncoated carbon particles can reach 31.3% when $\gamma = 0.2$, and correspondingly the Pt utilization ratio is 44.4%. When γ is higher than 0.5, all the carbon particles are coated with the Pt utilization ratio higher than 93.7%. For $\gamma = 0.3$, a majority of the ionomer thicknesses are around 2.5-5 nm, while the thin-film thicknesses are around 10-15 nm for $\gamma =1.1$. The ratio of f_{ion} relative to f_{Pt} drops greatly from 11.5 to 5.2 for γ ranging from 0.2 to 1.3. It is believed that all of the changes in the morphology of the CL with γ will affect $R_{\mathrm{H_2}}^{\mathrm{Pt}}$ to some extent. In the following analyses, we mainly focus on the results with γ higher than 0.5 since the coverage of ionomers over the Pt sites remains for percolation.

Fig. 7 Local transport resistance $R_{\mathrm{H_2}}^{\mathrm{Pt}}$ and the mass-weighted electro-chemical surface area a_{ECSA} versus ionomer to carbon ratio γ. Numerical predictions of different cases and the experimental data [28]

As γ increases, the ionomer thickness increases, resulting in higher R_{I}. The numerically predicted $R_{\mathrm{H_2}}^{\mathrm{Pt}}$ for all the cases increases with γ. The qualitative trend of $R_{\mathrm{H_2}}^{\mathrm{Pt}}$ with γ has also been experimentally observed by Spingler et al. [26] and Chowdhury et al. [66] who attributed the increase of $R_{\mathrm{H_2}}^{\mathrm{Pt}}$ to the thicker thin-film and Mashio et al. [67] who attributed the increase of R_{CL} to a change in the porosity. For Case 3 where the additional transport resistance mainly originated from R_{ads}, R_{I} increases with γ slightly due to the bulk permeation coefficient adopted. Besides, R_{ads} may decrease a little bit as f_{Pt} increases slightly. The tradeoff between these two effects results in the minimum variation of $R_{\mathrm{H_2}}^{\mathrm{Pt}}$ with γ. For Case 1 where the additional transport resistance mainly attributed to R_{dis}, the ratio of f_{ion} relative to f_{Pt} drops slightly, resulting in seemingly more resistive thin-film compared with the behavior of Case 3. For Case 5 where the additional transport resistance is completely attributed to R_{I}, the variation of $R_{H_2}^{Pt}$ with γ is most significant as R_I is influenced by γ directly. For Case 2 and 4 where the additional resistance attributed to a combination of the resistive thin-film and the interfacial transport resistances, the variations of $R_{H_2}^{Pt}$ with γ are just between those of Case 1 and 5. Comparing the numerically predicted data with the experimental results [28], the respective maximum deviations predicted with the input model parameters of Case 1 to 5 are 21%, 17%, 23%, 15% and 9.4%. Besides, the trend of the local transport resistance versus I/C ratio matches well the experimental data [28] with the input model parameters of Case 5. Therefore, it is considered to be more suitable to choose the input parameter of Case 5. This results suggest that the ionomer thin-film is more resistive than its bulk, which has also been addressed by Mashio et al. [25] that the reactant permeation coefficient in ionomer thin-films is 5 to 25% of its bulk. The result is also consistent with experimental and theoretical explorations of ionomer thin-films [9, 20, 21]. Therefore, the input model parameters of Case 5 are selected for the following studies.

Fig. 8 Structural parameters of the reconstructed CL for different ionomer to carbon ratios γ, left: thin-film volume fraction distribution; right: ratio of f_{ion} relative to f_{Pt}

3.3 Influence of Pt/C ratio, bare carbon fraction and porosity

Except for γ, the influences of other structural features of the CL on $R_{H_2}^{Pt}$, like the Pt/C ratio ω, bare carbon fraction ε_{bare} and porosity ε, have received less attention. As the reduction of L_{Pt} can be changed either by decreasing ω or l, and the decreasing of ω can be implemented either by dispersing less Pt particles on the carbon black or increasing the bare carbon fractions, the influences of ω and bare carbon fractions on $R_{H_2}^{Pt}$ and R_{CL} are crucial. The porosity can affect R_{Pore} directly since the diffusion process of the reactant is highly affected by the PSD. Besides, f_{ion} is also influenced by the porosity, which can also affect $R_{H_2}^{Pt}$. According to the reported experimental data, $R_{O_2}^{Pt}$ ranges from 100 to 1000 s·m^{-1} [5], and $R_{H_2}^{Pt}$ ranges from 900 to 2500 s·m^{-1} for different structural parameters of the CL [27, 28, 34].

Therefore, a thorough understanding of these parameters on $R_{H_2}^{Pt}$ and R_{CL} is important.

To study the influence of Pt/C ratio ω on $R_{H_2}^{Pt}$ and R_{CL}, the volume fractions of carbon and ionomer are kept as constant. γ is kept as 0.75 and l is 8 µm. The porosity of the CL only changes 3% for ω ranging from 18.3 to 50%. The following analyses indicate that such a small variation of porosity on the influence of $R_{H_2}^{Pt}$ and R_{CL} can be ignored. Detailed structural parameters of the CL are provided in Table S3. Fig. 9 shows the variations of $R_{H_2}^{Pt}$ and R_{CL} versus ω. As can be seen, $R_{H_2}^{Pt}$ increases with ω, showing the same qualitative trend with Owejan et al. [17]. As addressed by Yoon and Weber [68], even though the transport pathways become longer for low ω, the reactant flux to discrete Pt particles increases since the interfacial surface area of ionomer/pore per Pt particle increases [28]. Therefore, the utilization of Pt increases with the decrease of ω. $R_{H_2}^{Pt}$ increases from 1866 to 2770 $s \cdot m^{-1}$ for ω ranging from 18.3 to 50%. As expected, R_{CL} decreases with ω since L_{Pt} increases with ω. However, R_{CL} only changes 2% for ω ranging from 45 to 50%. Our result has also been experimentally observed that R_{CL} is insensitive to a further increasing L_{Pt} with higher ω (see Fig. 3 in ref. [17]). This is interesting as a tradeoff between the fuel cell performance and the cost needs to be considered for the design of the low-loaded CL.

Fig. 9 Variations of the local transport resistance $R_{H_2}^{Pt}$ and R_{CL} with Pt/C ratios, the structural parameters are $\gamma = 0.75$ and $\varepsilon=0.55$

For better understanding of the influence of ω on $R_{H_2}^{Pt}$, one Pt/C particle coated with the ionomer thin-film is simulated and shown in Fig. 10. It can be found that the distribution of the hydrogen concentration in the ionomer only changes slightly for ω ranging from 30 to 60%. This figure also presents a_{ECSA} and the ratio of f_{ion} and f_{Pt} versus ω. f_{Pt} increases with ω while f_{ion} remains constant as only the volume fraction of Pt changes, and therefore the ratio of f_{ion} relative to f_{Pt} decreases. Besides, a_{ECSA} decreases from 72.3 to 59.6 $m^2 \cdot g^{-1}{}_{Pt}$. The numerically predicted trend of a_{ECSA} versus ω agrees well with the experimental result conducted by Owejan et al. [17] that the roughness factor decreased from 21.99 to 15.12 m_{Pt}^2 m_{MEA}^{-2} as ω increased from 10% to 50% for the same L_{Pt}. The reason is as follows. The volume fraction of Pt in the present work increases from 0.005 to 0.0213 for the value of ω ranging from 18.3 to 50%. Meanwhile, the volume fraction of ionomer decreases slightly from 0.179 to 0.172. Note that only the Pt surfaces contacting with ionomer and carbon are considered as the reaction sites (see Section 2.2), the roughness factor increases with ω for the same CL thickness we adopted. However, more surfaces of Pt particles will become inactive since the volume fraction of ionomer is comparatively low. Besides, the increasing Pt particles on per primary carbon particles may contact with each other. Therefore, a_{ECSA} decreased with ω.

Fig. 10 Variations of the structural parameters a_{ECSA} and the ratio of f_{ion} and f_{Pt} versus Pt/C ratio ω

The effect of bare carbon fraction ε_{bare} on $R_{H_2}^{Pt}$ is shown in Fig. 11. Detailed structural parameters are: γ = 0.75, l=8 μm, L_{Pt} =0.075 mg·cm^{-2}, and ε=0.55 (see Table S4). As the volume fraction of the diluted carbons without Pt particles ranges from 0 to 50%, the corresponding Pt/C ratio ω of the non-diluted Pt/C particles ranges from 18.3 to 36.6%. It can be found that $R_{H_2}^{Pt}$ increases with ε_{bare} as expected, which is similar with the effect of ω. Our result agrees well with Owejan et al. [17], who experimentally found that R_{CL} increases with ε_{bare} for a given L_{Pt} of 0.025 mg·cm^{-2}. This indicates that Pt particles should be dispersed uniformly on the primary particles. Combined with the effect of ω on $R_{H_2}^{Pt}$, it can be concluded that the reduction of L_{Pt} by changing l rather than the carbon dilution fraction is preferable.

Fig. 11 Variations of the local transport resistance $R_{H_2}^{Pt}$ versus the volume fractions of the bare carbon, ε_{bare}, the structural parameters are γ= 0.75 and ε=0.55, l=8μm

The influence of ε on $R_{H_2}^{Pt}$ and R_{CL} is shown in Fig. 12. The structural parameters are

γ=0.75, l=8 μm, and ω =18.3%. L_{Pt} decreases with ε linearly from 0.117 to 0.067 mg·cm^{-2}. Detailed structural parameters are given in Table S5. Table 3 lists the variations of f_{ion} and f_{Pt} for different porosities. The ratio of f_{ion} relative to f_{Pt} increases from 4.3 to 6.1 for ε ranging from 0.3 to 0.6. As seen in the figure, $R_{H_2}^{Pt}$ decreases from 2247 to 1860 s·m^{-1} with ε, which is mainly due to the increasing ratio of f_{ion} relative to f_{Pt}. R_{CL} increases with ε as f_{Pt} decreases with ε. Table 1 also lists the numerically predicted $D_{H_2}^{eff}$ for different porosities. For a typical pore size of 200 nm, the calculated $D_{H_2:mix}$ with Eq. (9) is 4.9×10^{-5} m^2·s^{-1}. It can be seen that $D_{H_2}^{eff}$ is about one-order-magnitude lower than $D_{H_2:mix}$ with the detailed PSD considered. To compare the numerical predicted $D_{H_2}^{eff}$ with the previously reported values, the formation factor F, defined as the ratio between the effective diffusivity and the molecular diffusivity, is adopted. As depicted in Fig. 13, our data are slightly higher than that given by Sabharwal et al. [55] and Siddique and Liu [42], while matches well with the data given by Fathi et al. [69]. Note that in the above references, the Knudsen diffusivity of oxygen is used, which is smaller than that of hydrogen simulated in the present work. As pointed out by Sabharwal et al. [55], the PSD was overestimated in the work of Fathi et al. [69]. A tradeoff between the higher mean pore size and the lower Knudsen diffusivity results in high accordance of their data with our results.

As shown in Fig. 12, the numerically predicted R_{Pore} decreases from 1.223 to 0.236 s·m^{-1}, indicating the contribution of the pores to R_{CL} is comparatively small. To further validate the numerical obtained R_{Pore}, analytical expressions in Eqs. (2) and (3) are adopted and the calculated results are also listed in Table 3. The maximum deviation between the numerically predicted R_{Pore} and the analytical data are 23%. This result is acceptable since the analytical solutions are based on the assumption that the reaction rate j along the thickness direction is proportional to c_p, which is different from that shown in Fig. 5(b). It can be inferred from Eq. (3) that R_{Pore} turns to be more significant for lower porosity and thicker CL.

Fig. 12 Variations of the local transport resistance $R_{H_2}^{Pt}$ *and* R_{CL} *with porosity* ε*, the structural parameters are* γ = 0.75, l =8.0μm *and* ω=18.3%

Fig. 13 Comparison of the formation factor with the previously published studies [42, 55, 69]

Table 3 Comparison of the predicted R_{Pore} with the analytical results for the structural parameters of $\gamma = 0.75$, $l = 8.0\mu m$ and $\omega = 18.3\%$

4. Conclusions

The experimentally observed hydrogen-transport resistance in the CL of a PEFC was simulated using a mesoscopic model with the proposed interfacial conditions treatments at ionomer/pore and Pt/ionomer surfaces. This method fully considered the transport process of hydrogen and proton in the microstructures of a reconstructed CL. Distributions of the primary particle size, ionomer thickness, pore size, Pt-mass-specific electrochemical surface area and roughness factor were characterized. Limiting current densities of the CL with different structural parameters were obtained and correspondingly the local transport resistance $R_{\mathrm{H_2}}^{\mathrm{Pt}}$, catalyst layer resistance R_{CL} and pore resistance R_{Pore} were calculated.

Detailed analyses suggested that the resistance of the ionomer thin-film assuming the transport properties of the bulk ionomer underestimates the local transport resistance, $R_{\mathrm{H_2}}^{\mathrm{Pt}}$. Parameter sensitivity analyses on the permeation coefficient and interfacial transport resistances revealed that the dissolution resistances, adsorption resistance and the diffusion resistance are fully coupled. The dissolution and adsorption resistances are underestimated with the traditional expressions without considering the real microstructure of the CL. The local transport resistance is mainly attributed to the diffusion resistance of the ionomer thin-film, which is more resistive with its permeation coefficient fitted to be 5.9% of its bulk value.

The local transport resistance increases with I/C ratio γ due to the thicker ionomer coated on the Pt/C particles. A trade-off between the increasing local transport resistance and decreasing catalyst layer resistance with Pt/C ratio ω should be made. Pt particles should be dispersed more uniformly as the local transport resistance increases with the bare carbon fractions due to the decreasing surface area for reactant flux per Pt particle. The local transport resistance decreases with porosity as the ratio of the ionomer loading relative to Pt increases. The contribution of R_{Pore} to R_{CL} is comparatively small, and R_{Pore} decreases with the porosity as the effective diffusivity increases. The present work on $R_{\mathrm{H_2}}^{\mathrm{Pt}}$ is analogous to $R_{\mathrm{O_2}}^{\mathrm{Pt}}$, and future work on the permeation coefficient of the reactant species in the ionomer thin-film for different operation conditions is highlighted. More experiments are needed to help unravel the origin of the additional voltage loss for low-loaded CL.

Supporting information

Supplementary data associated with this article can be found in the online version.

Acknowledgements

We would like to thank Anamika Chowdhury for critical comments and discussion. This work was supported by the National Natural Science Foundation of China (51806170), the National Postdoctoral Program for Innovative Talents (BX201700190) and the National Postdoctoral Program Foundation of China (2017M620450). This work was also supported by the Fuel Cell Technologies Office (FCTO), and Office of Energy Efficiency and Renewable Energy (EERE).

References

1. Stephens, I.E.L., J. Rossmeisl, and I. Chorkendorff, *Toward sustainable fuel cells.* Science, 2016. **354**(6318): p. 1378-1379.
2. Vasile, N.S., R. Doherty, A.H.A. Monteverde Videla, and S. Specchia, *3D multi-physics modeling of a gas diffusion electrode for oxygen reduction reaction for electrochemical energy conversion in PEM fuel cells.* Applied Energy, 2016. **175**: p. 435-450.
3. Wang, Y., K.S. Chen, J. Mishler, S.C. Cho, and X.C. Adroher, *A review of polymer electrolyte membrane fuel cells: Technology, applications, and needs on fundamental research.* Applied Energy, 2011. **88**(4): p. 981-1007.
4. Orfanidia, A., P. Madkikara, H.A. El-Sayeda, G.S. Harzera, T. Kratkyb, and H.A. Gasteiger, *The Key to High Performance Low Pt Loaded Electrodes.* Journal of The Electrochemical Society, 2017. **164**(4): p. F418-F426.
5. Weber, A.Z. and A. Kusoglu, *Unexplained transport resistances for low-loaded fuel-cell catalyst layers.* J. Mater. Chem. A, 2014. **2**(41): p. 17207-17211.
6. Kongkanand, A. and M.F. Mathias, *The Priority and Challenge of High-Power Performance of Low-Platinum Proton-Exchange Membrane Fuel Cells.* J Phys Chem Lett, 2016. **7**(7): p. 1127-37.
7. Banham, D. and S. Ye, *Current Status and Future Development of Catalyst Materials and Catalyst Layers for Proton Exchange Membrane Fuel Cells: An Industrial Perspective.* ACS Energy Letters, 2017. **2**(3): p. 629-638.
8. Greszler, T.A., D. Caulk, and P. Sinha, *The impact of platinum loading on oxygen transport resistance.* Journal of The Electrochemical Society, 2012. **159**(12): p. F831-F840.
9. Kusoglu, A. and A.Z. Weber, *New Insights into Perfluorinated Sulfonic-Acid Ionomers.* Chem Rev, 2017. **117**(3): p. 987-1104.
10. Jinnouchi, R., K. Kodama, A. Nagoya, and Y. Morimoto, *Simulated Volcano Plot of Oxygen Reduction Reaction on Stepped Pt Surfaces.* Electrochimica Acta, 2017. **230**: p. 470-478.
11. Vanya, P., J. Sharman, and J.A. Elliott, *Mesoscale simulations of confined Nafion thin films.* J Chem Phys, 2017. **147**(21): p. 214904.
12. Modestino, M.A., D.K. Paul, S. Dishari, S.A. Petrina, F.I. Allen, M.A. Hickner, K. Karan, R.A. Segalman, and A.Z. Weber, *Self-Assembly and Transport Limitations in Confined Nafion Films.* Macromolecules, 2013. **46**(3): p. 867-873.
13. Page, K.A., A. Kusoglu, C.M. Stafford, S. Kim, R.J. Kline, and A.Z. Weber, *Confinement-driven increase in ionomer thin-film modulus.* Nano Lett, 2014. **14**(5): p. 2299-304.
14. Kusoglu, A., T.J. Dursch, and A.Z. Weber, *Nanostructure/Swelling Relationships of Bulk and Thin-Film PFSA Ionomers.* Advanced Functional Materials, 2016. **26**(27): p. 4961-4975.
15. Tesfaye, M., D.I. Kushner, B.D. McCloskey, A.Z. Weber, and A. Kusoglu, *Thermal Transitions in Perfluorosulfonated Ionomer Thin-Films.* ACS Macro Letters, 2018. **7**(10): p. 1237-1242.
16. Suzuki, A., U. Sen, T. Hattori, R. Miura, R. Nagumo, H. Tsuboi, N. Hatakeyama, A. Endou, H. Takaba, M.C. Williams, and A. Miyamoto, *Ionomer content in the catalyst layer of polymer electrolyte membrane fuel cell (PEMFC): effects on diffusion and performance.* International Journal of Hydrogen Energy, 2011. **36**(3): p. 2221-2229.
17. Owejan, J.P., J.E. Owejan, and W. Gu, *Impact of platinum loading and catalyst layer structure on PEMFC performance.* Journal of The Electrochemical Society, 2013. **160**(8): p. F824-F833.
18. Kudo, K., R. Jinnouchi, and Y. Morimoto, *Humidity and Temperature Dependences of Oxygen Transport Resistance of Nafion Thin Film on Platinum Electrode.* Electrochimica Acta, 2016. **209**: p. 682-690.

19. Liu, H., W.K. Epting, and S. Litster, *Gas transport resistance in polymer electrolyte thin films on oxygen reduction reaction catalysts.* Langmuir, 2015. **31**(36): p. 9853-9858.

20. Suzuki, T., H. Yamada, K. Tsusaka, and Y. Morimoto, *Modeling of Oxygen Diffusion Resistance in Polymer Electrolyte Fuel Cells in the Intermediate Potential Region.* Journal of The Electrochemical Society, 2018. **165**(3): p. F166-172.

21. Jinnouchi, R., K. Kudo, N. Kitano, and Y. Morimoto, *Molecular Dynamics Simulations on O_2 Permeation through Nafion Ionomer on Platinum Surface.* Electrochimica Acta, 2016. **188**: p. 767-776.

22. Mu, Y.-T., P. He, J. Ding, L. Chen, and W.-Q. Tao, *Numerical Study of the Gas Purging Process of a Proton Exchange Membrane Fuel Cell.* Energy Procedia, 2017. **105**: p. 1967-1973.

23. Nonoyama, N., S. Okazaki, A.Z. Weber, Y. Ikogi, and T. Yoshida, *Analysis of oxygen-transport diffusion resistance in proton-exchange-membrane fuel cells.* Journal of The Electrochemical Society, 2011. **158**(4): p. B416-B423.

24. Muzaffar, T., T. Kadyk, and M. Eikerling, *Tipping water balance and the Pt loading effect in polymer electrolyte fuel cells: a model-based analysis.* Sustainable Energy & Fuels, 2018. **2**(6): p. 1189-1196.

25. Mashio, T., H. Iden, A. Ohma, and T. Tokumasu, *Modeling of local gas transport in catalyst layers of PEM fuel cells.* Journal of Electroanalytical Chemistry, 2017. **790**: p. 27-39.

26. Spingler, F.B., A. Phillips, T. Schuler, M.C. Tucker, and A.Z. Weber, *Investigating fuel-cell transport limitations using hydrogen limiting current.* International Journal of Hydrogen Energy, 2017. **42**(19): p. 13960-13969.

27. Freiberg, A.T.S., M.C. Tucker, and A.Z. Weber, *Polarization loss correction derived from hydrogen local-resistance measurement in low Pt-loaded polymer-electrolyte fuel cells.* Electrochemistry Communications, 2017. **79**: p. 14-17.

28. Schuler, T., A. Chowdhury, A.T.S. Freiberg, B. Sneed, F.B. Spingler, M.C. Tucker, K.L. More, C.J. Radke, and A.Z. Weber, *Fuel-cell catalyst-layer resistance via hydrogen limiting-current measurements.* Journal of The Electrochemical Society, 2019. **166**(7): p. F3020-F3031.

29. Moore, M., P. Wardlaw, P. Dobson, J.J. Boisvert, A. Putz, R.J. Spiteri, and M. Secanell, *Understanding the Effect of Kinetic and Mass Transport Processes in Cathode Agglomerates.* Journal of The Electrochemical Society, 2014. **161**(8): p. E3125-E3137.

30. Kulikovsky, A.A., *Polarization curve of a PEM fuel cell with the account of a finite rate of oxygen adsorption on Pt surface.* International Journal of Hydrogen Energy, 2014. **39**(33): p. 19018-19023.

31. Hao, L., K. Moriyama, W. Gu, and C.-Y. Wang, *Modeling and Experimental Validation of Pt Loading and Electrode Composition Effects in PEM Fuel Cells.* Journal of The Electrochemical Society, 2015. **162**(8): p. F854-F867.

32. Jiang, J., Y. Li, J. Liang, W. Yang, and X. Li, *Modeling of high-efficient direct methanol fuel cells with order-structured catalyst layer.* Applied Energy, 2019. **252**: p. 113431.

33. Zhang, R., T. Min, L. Chen, Q. Kang, Y.-L. He, and W.-Q. Tao, *Pore-scale and multiscale study of effects of Pt degradation on reactive transport processes in proton exchange membrane fuel cells.* Applied Energy, 2019. **253**: p. 113590.

34. Darling, R., *A Comparison of Models for Transport Resistance in Fuel-Cell Catalyst Layers.* Journal of The Electrochemical Society, 2018. **165**(16): p. F1331-F1339.

35. Oh, H., Y.i. Lee, G. Lee, K. Min, and J.S. Yi, *Experimental dissection of oxygen transport resistance in the components of a polymer electrolyte membrane fuel cell.* Journal of Power Sources, 2017. **345**: p. 67-77.

36. Suzuki, T., K. Kudo, and Y. Morimoto, *Model for investigation of oxygen transport limitation in a polymer electrolyte fuel cell.* Journal of Power Sources, 2013. **222**: p. 379-389.

37. Cetinbas, F.C., X. Wang, R.K. Ahluwalia, N.N. Kariuki, R. Winarski, Z. Yang, J. Sharman, and D.J. Myers,

Microstructural Analysis and Transport Resistances of Low-Platinum-Loaded PEFC Electrodes. Journal of The Electrochemical Society, 2017. **164**(14): p. F1595-1607.

38. Lange, K.J., P.-C. Sui, and N. Djilali, *Pore scale modeling of a proton exchange membrane fuel cell catalyst layer: effects of water vapor and temperature.* Journal of Power Sources, 2011. **196**(6): p. 3195-3203.
39. Zhang, X., Y. Gao, H. Ostadi, K. Jiang, and R. Chen, *Method to improve catalyst layer model for modelling proton exchange membrane fuel cell.* Journal of Power Sources, 2015. **289**: p. 114-128.
40. Sabharwal, M., L.M. Pant, A. Putz, D. Susac, J. Jankovic, and M. Secanell, *Analysis of catalyst layer microstructures: from imaging to performance.* Fuel Cells, 2016. **16**(6): p. 734-753.
41. Chen, L., G. Wu, E.F. Holby, P. Zelenay, W.-Q. Tao, and Q. Kang, *Lattice Boltzmann pore-scale investigation of coupled physical-electrochemical processes in C/Pt and non-precious metal cathode catalyst layers in proton exchange membrane fuel cells.* Electrochimica Acta, 2015. **158**: p. 175-186.
42. Siddique, N.A. and F. Liu, *Process based reconstruction and simulation of a three-dimensional fuel cell catalyst layer.* Electrochimica Acta, 2010. **55**(19): p. 5357-5366.
43. Hou, Y., H. Deng, F. Pan, W. Chen, Q. Du, and K. Jiao, *Pore-scale investigation of catalyst layer ingredient and structure effect in proton exchange membrane fuel cell.* Applied Energy, 2019. **253**: p. 113561.
44. Hwang, G.S. and A.Z. Weber, *Effective-Diffusivity Measurement of Partially-Saturated Fuel-Cell Gas-Diffusion Layers.* Journal of The Electrochemical Society, 2012. **159**(11): p. F683-F692.
45. Baker, D.R., D.A. Caulk, K.C. Neyerlin, and M.W. Murphy, *Measurement of oxygen transport resistance in PEM fuel cells by limiting current methods.* Journal of The Electrochemical Society, 2009. **156**(9): p. B991-B1003.
46. Mu, Y.-T., P. He, J. Ding, and W.-Q. Tao, *Modeling of the operation conditions on the gas purging performance of polymer electrolyte membrane fuel cells.* International Journal of Hydrogen Energy, 2017. **42**(16): p. 11788-11802.
47. Perry, R.B. and D.W. Green, *Perry's Chemical Engineers' Handbook*. 1999, New York: McGraw-Hill.
48. Weber, A.Z. and J. Newman, *Transport in Polymer-Electrolyte Membranes II. Mathematical Model.* Journal of The Electrochemical Society, 2004. **151**(2): p. A311-325.
49. Wang, J.X., T.E. Springer, and R.R. Adzic, *Dual-Pathway Kinetic Equation for the Hydrogen Oxidation Reaction on Pt Electrodes.* Journal of The Electrochemical Society, 2006. **153**(9): p. A1732-A1740.
50. Mu, Y.-T., L. Chen, Y.-L. He, Q.-J. Kang, and W.-Q. Tao, *Nucleate boiling performance evaluation of cavities at mesoscale level.* International Journal of Heat and Mass Transfer, 2017. **106**: p. 708-719.
51. Mu, Y.-T., L. Chen, Y.-L. He, and W.-Q. Tao, *Pore-scale modelling of dynamic interaction between SVOCs and airborne particles with lattice Boltzmann method.* Building and Environment, 2016. **104**: p. 152-161.
52. Mu, Y.-T., Z.-L. Gu, P. He, and W.-Q. Tao, *Lattice Boltzmann method for conjugated heat and mass transfer with general interfacial conditions.* Physical Review E, 2018. **98**(4).
53. Wang, G., P.P. Mukherjee, and C.-Y. Wang, *Direct numerical simulation (DNS) modeling of PEFC electrodes.* Electrochimica Acta, 2006. **51**(15): p. 3151-3160.
54. Kim, S.H. and H. Pitsch, *Reconstruction and Effective Transport Properties of the Catalyst Layer in PEM Fuel Cells.* Journal of The Electrochemical Society, 2009. **156**(6): p. B673.
55. Sabharwal, M., L.M. Pant, N. Patel, and M. Secanell, *Computational Analysis of Gas Transport in Fuel Cell Catalyst Layer under Dry and Partially Saturated Conditions.* Journal of The Electrochemical Society, 2019. **166**(7): p. F3065-F3080.
56. Ishikawa, H., Y. Sugawara, G. Inoue, and M. Kawase, *Effects of Pt and ionomer ratios on the structure of catalyst layer: A theoretical model for polymer electrolyte fuel cells.* Journal of Power Sources, 2018. **374**: p. 196-204.
57. Malek, K., T. Mashio, and M. Eikerling, *Microstructure of Catalyst Layers in PEM Fuel Cells Redefined: A*

Computational Approach. Electrocatalysis, 2011. **2**(2): p. 141-157.

58. Cetinbas, F.C., R.K. Ahluwalia, N. Kariuki, V. De Andrade, D. Fongalland, L. Smith, J. Sharman, P. Ferreira, S. Rasouli, and D.J. Myers, *Hybrid approach combining multiple characterization techniques and simulations for microstructural analysis of proton exchange membrane fuel cell electrodes.* Journal of Power Sources, 2017. **344**: p. 62-73.

59. Haug, A., *Novel ionomers and electrode structures for improved PEMFC electrode performance at low PGM loadings*, in *Annual Merit Review and Evaluation Meeting*. 2018, DOE Hydrogen and Fuel Cells Program: Washington, DC.

60. Yu, Z., R.N. Carter, and J. Zhang, *Measurements of Pore Size Distribution, Porosity, Effective Oxygen Diffusivity, and Tortuosity of PEM Fuel Cell Electrodes.* Fuel Cells, 2012. **12**(4): p. 557-565.

61. Ihonen, J., F.d.r. Jaouen, G.r. Lindbergh, A. Lundblad, and G.r. Sundholm, *Investigation of Mass-Transport Limitations in the Solid Polymer Fuel Cell Cathode.* Journal of The Electrochemical Society, 2002. **149**(4): p. A448-A454.

62. Ozden, A., S. Shahgaldi, X. Li, and F. Hamdullahpur, *The impact of ionomer type on the morphological and microstructural degradations of proton exchange membrane fuel cell electrodes under freeze-thaw cycles.* Applied Energy, 2019. **238**: p. 1048-1059.

63. Soboleva, T., X. Zhao, K. Malek, Z. Xie, T. Navessin, and S. Holdcroft, *On the micro-, meso-, and macroporous structures of polymer electrolyte membrane fuel cell catalyst layers.* ACS Appl Mater Interfaces, 2010. **2**(2): p. 375-84.

64. Lange, K.J., P.-C. Sui, and N. Djilali, *Pore Scale Simulation of Transport and Electrochemical Reactions in Reconstructed PEMFC Catalyst Layers.* Journal of The Electrochemical Society, 2010. **157**(10): p. B1434.

65. Jomori, S., N. Nonoyama, and T. Yoshida, *Analysis and modeling of PEMFC degradation: Effect on oxygen transport.* Journal of Power Sources, 2012. **215**: p. 18-27.

66. Chowdhury, A., C.J. Radke, and A.Z. Weber, *Transport Resistances in Fuel-Cell Catalyst Layers.* ECS Transactions, 2017. **80**(8): p. 321-333.

67. Mashio, T., A. Ohma, S. Yamamoto, and K. Shinohara, *Analysis of Reactant Gas Transport in a Catalyst Layer.* ECS Transactions, 2007. **11**(1): p. 529-540.

68. Yoon, W. and A.Z. Weber, *Modeling Low-Platinum-Loading Effects in Fuel-Cell Catalyst Layers.* Journal of The Electrochemical Society, 2011. **158**(8): p. B1007-B1018.

69. Fathi, H., A. Raoof, S. Mansouri, and M.T. van Genuchten, *Effects of porosity and water saturation on the effective diffusivity of a cathode catalyst layer.* Journal of The Electrochemical Society, 2017. **164**(4): p. F298-F305.

Figure Captions

Fig. 1 Schematic illustration of the transport process of hydrogen in a hydrogen-pump experiment

Fig. 2 Schematic description of the lattice nodes and its numerical treatment, (a) treatment of the conjugated mass transfer between the pore and ionomer; (b) treatment of the chemical reaction at the platinum surfaces

Fig. 3 Comparisons of the numerical reconstructed CL with the existing data [58], (a) morphology of the reconstructed CL (pore: white, carbon: black, platinum: red, ionomer: cyan); (b) normalized volume fractions of all the components of the CL along the thickness direction; (c) primary particle size number and ionomer thin-film thickness distributions; (d) pore size distribution. The structural parameters of the CL are $\gamma = 0.8$, $\varepsilon = 0.42$, $l = 3.75$ μm, $L_{\mathrm{Pt}} = 0.092$ mg·cm^{-2}, and $\omega = 30\%$.

Fig. 4 Comparison of the transport resistance R_{CL} between numerical data and the experimental data [28] versus platinum loadings L_{Pt} and roughness factors f_{Pt}

Fig. 5 Illustrations of the hydrogen concentration and chemical reaction rate in the catalyst layer at the cross-section of y=150 nm. (a) contours of c_{p} in pore, c_{ion} in ionomer, η in ionomer and chemical reaction rate j at platinum surfaces; (b) variations of c_{p}, c_{ion}, η and j along the thickness direction. The structural parameters are: $\gamma=0.75$, $\varepsilon=0.55$, $l=4.68$ μm, $L_{\mathrm{Pt}}=0.05$mg·cm^{-2}, and $\omega=18.3\%$.

Fig. 6 Parameter sensitivity analyses of the hydrogen permeation coefficient, dissolution reaction rate and adsorption reaction rate on the local transport resistance $R_{\mathrm{H_2}}^{\mathrm{Pt}}$

Fig. 7 Local transport resistance $R_{\mathrm{H_2}}^{\mathrm{Pt}}$ and the mass-weighted electro-chemical surface area a_{ECSA} versus ionomer to carbon ratios γ. Numerical predictions of different cases and the experimental data [28]

Fig. 8 Structural parameters of the reconstructed CL for different ionomer to carbon ratio γ, left: thin-film volume fraction distribution; right: ratio of f_{ion} relative to f_{Pt}

Fig. 9 Variations of the local transport resistance $R_{\mathrm{H_2}}^{\mathrm{Pt}}$ and R_{CL} with Pt/C ratios, the structural parameters are $\gamma = 0.75$ and $\varepsilon=0.55$

Fig. 10 Variations of the structural parameters a_{ECSA} and the ratio of f_{ion} and f_{Pt} versus Pt/C ratio ω

Fig. 11 Variations of the local transport resistance $R_{\mathrm{H_2}}^{\mathrm{Pt}}$ versus the volume fractions of the bare carbon, $\varepsilon_{\mathrm{bare}}$, the structural parameters are $\gamma= 0.75$ and $\varepsilon=0.55$, $l=8\mu\mathrm{m}$

Fig. 12 Variations of the local transport resistance $R_{\mathrm{H_2}}^{\mathrm{Pt}}$ and R_{CL} with porosity ε, the structural parameters are $\gamma = 0.75$, $l = 8.0\mu\mathrm{m}$ and $\omega=18.3\%$

Fig. 13 Comparison of the formation factor with the previously published studies [42, 55, 69]

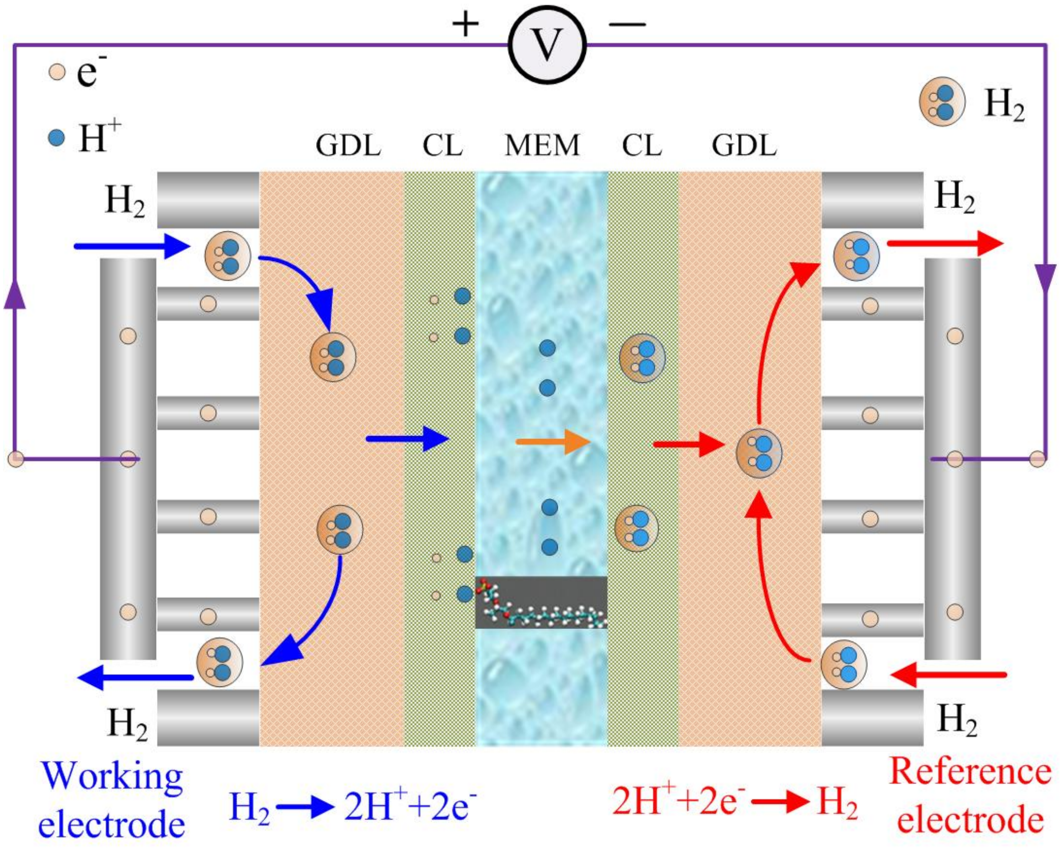

Fig. 1 Schematic illustration of the transport process of hydrogen in a hydrogen-pump experiment

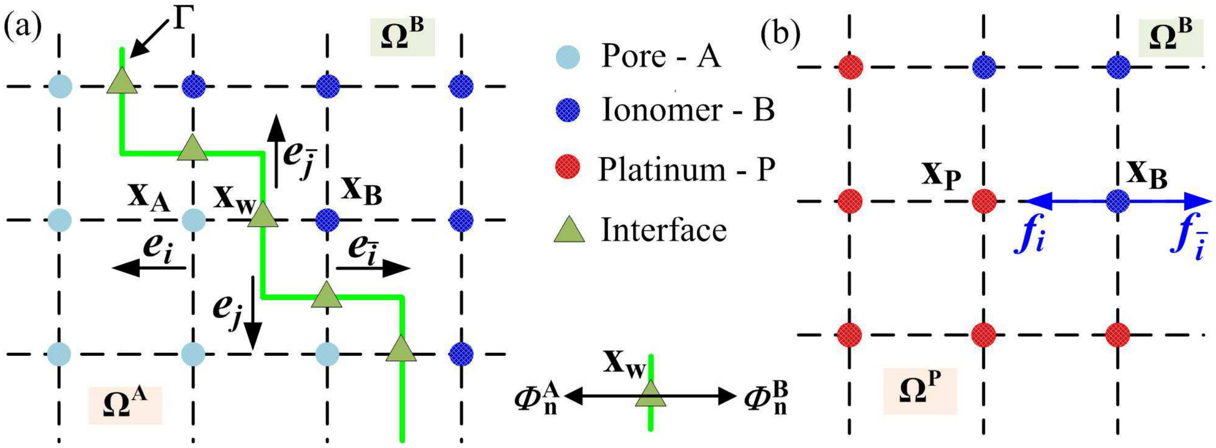

Fig. 2 Schematic description of the lattice nodes and its numerical treatment, (a) treatment of the conjugated mass transfer between the pore and ionomer; (b) treatment of the chemical reaction at the platinum surfaces

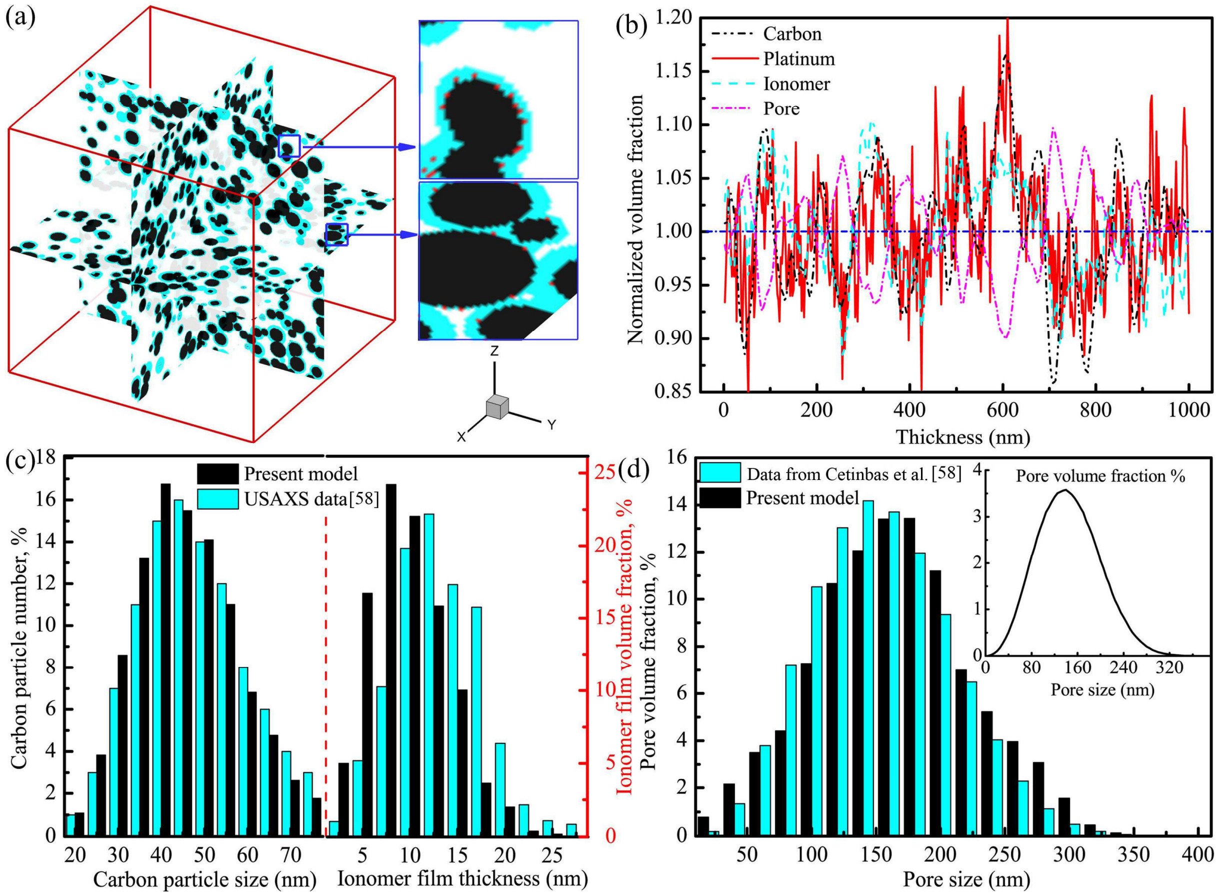

Fig. 3 Comparisons of the numerical reconstructed CL with the existing data [58], (a) morphology of the reconstructed CL (pore: white, carbon: black, platinum: red, ionomer: cyan); (b) normalized volume fractions of all the components of the CL along the thickness direction; (c) primary particle size number and ionomer thin-film thickness distributions; (d) pore size distribution. The structural parameters of the CL are $\gamma = 0.8$, $\varepsilon = 0.42$, l =3.75 μm, L_{Pt} =0.092 mg·cm^{-2}, ω=30%.

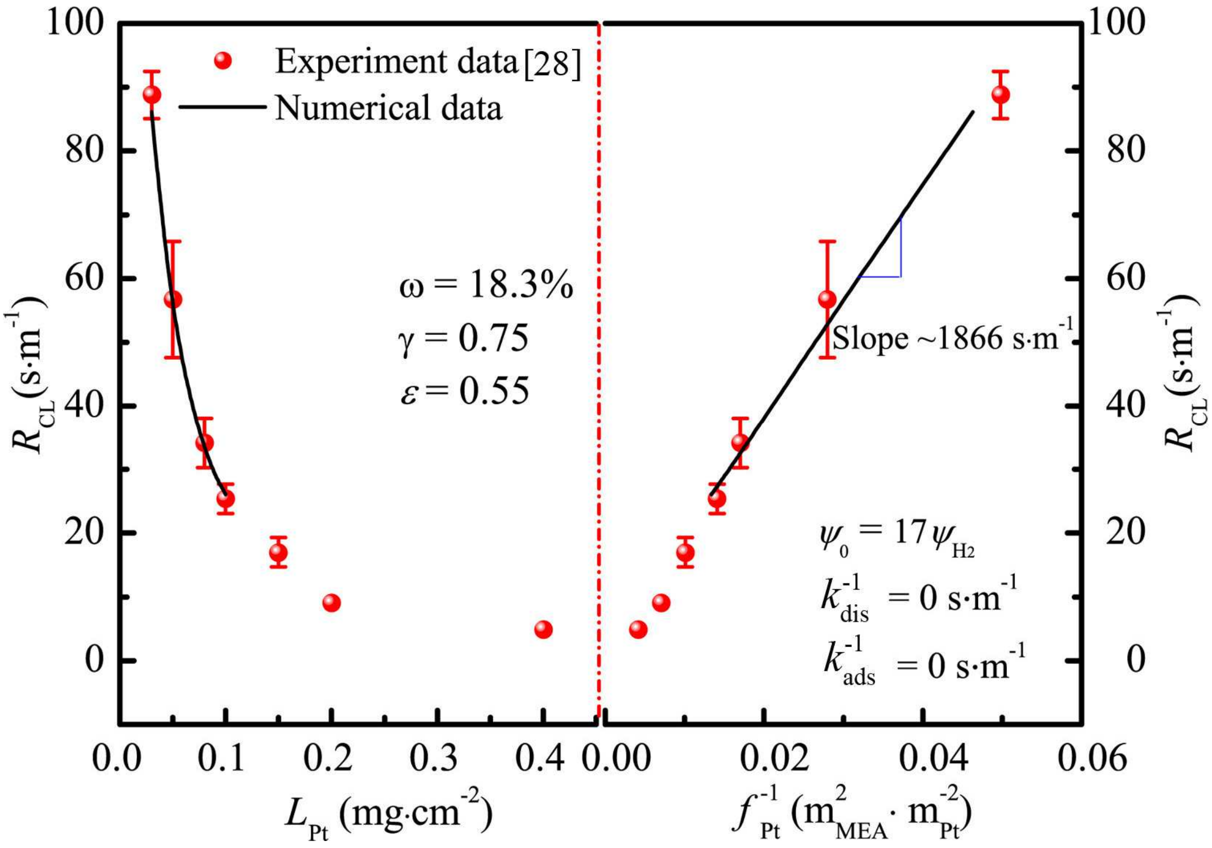

Fig. 4 Comparison of the transport resistance R_{CL} between numerical data and the experimental data [28] versus platinum loadings L_{Pt} and roughness factors f_{Pt}

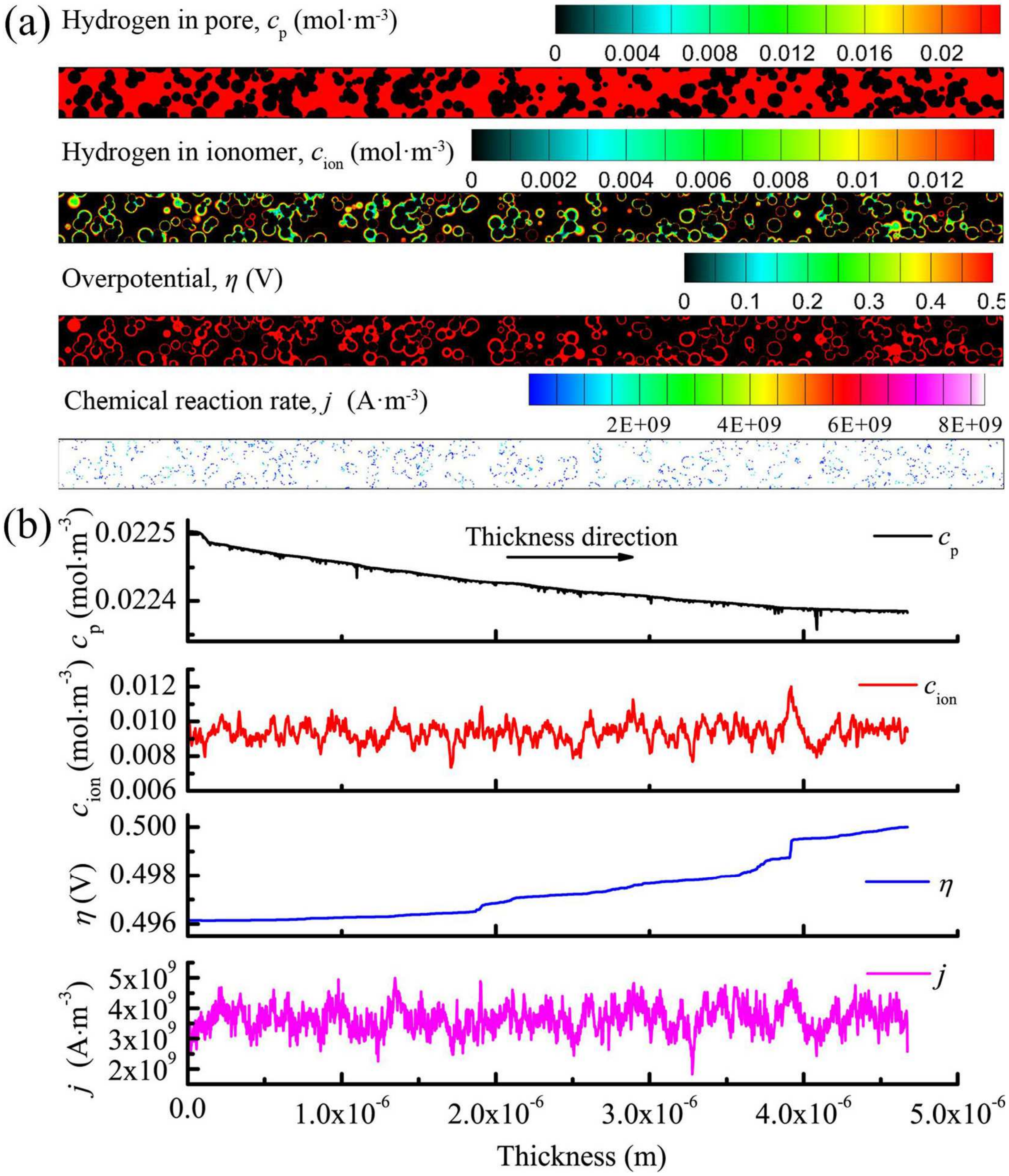

Fig. 5 Illustrations of the hydrogen concentration and chemical reaction rate in the catalyst layer at the cross-section of y=150 nm. (a) contours of c_p in pore, c_{ion} in ionomer, η in ionomer and chemical reaction rate j at platinum surfaces; (b) variations of c_p, c_{ion}, η and j along the thickness direction. The structural parameters are: γ=0.75, ε=0.55, l=4.68 μm, L_{Pt}=0.05mg·cm^{-2}, and ω=18.3%.

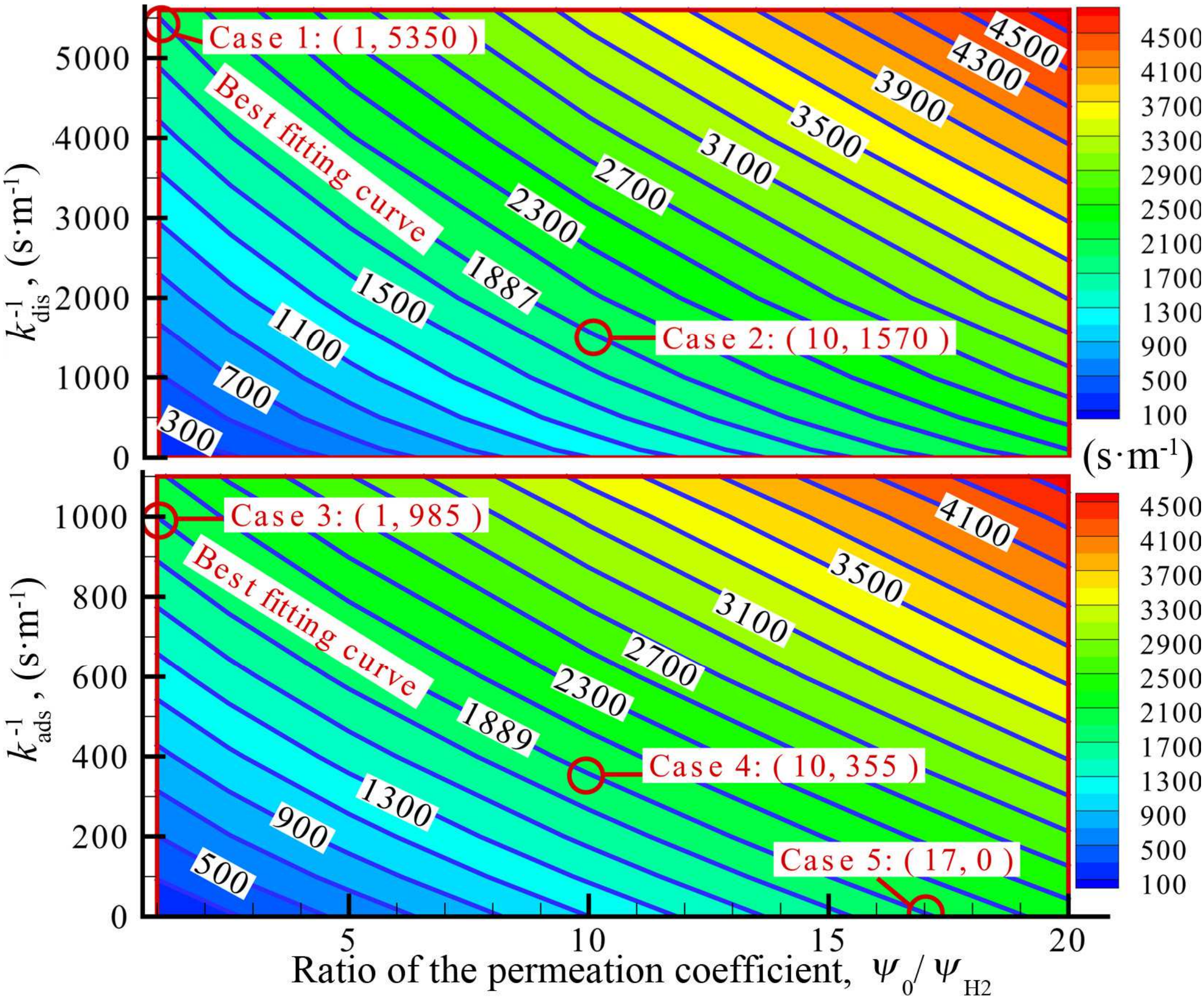

Fig. 6 Parameter sensitivity analyses of the hydrogen permeation coefficient, dissolution reaction rate and adsorption reaction rate on the local transport resistance $R_{\mathrm{H_2}}^{\mathrm{Pt}}$

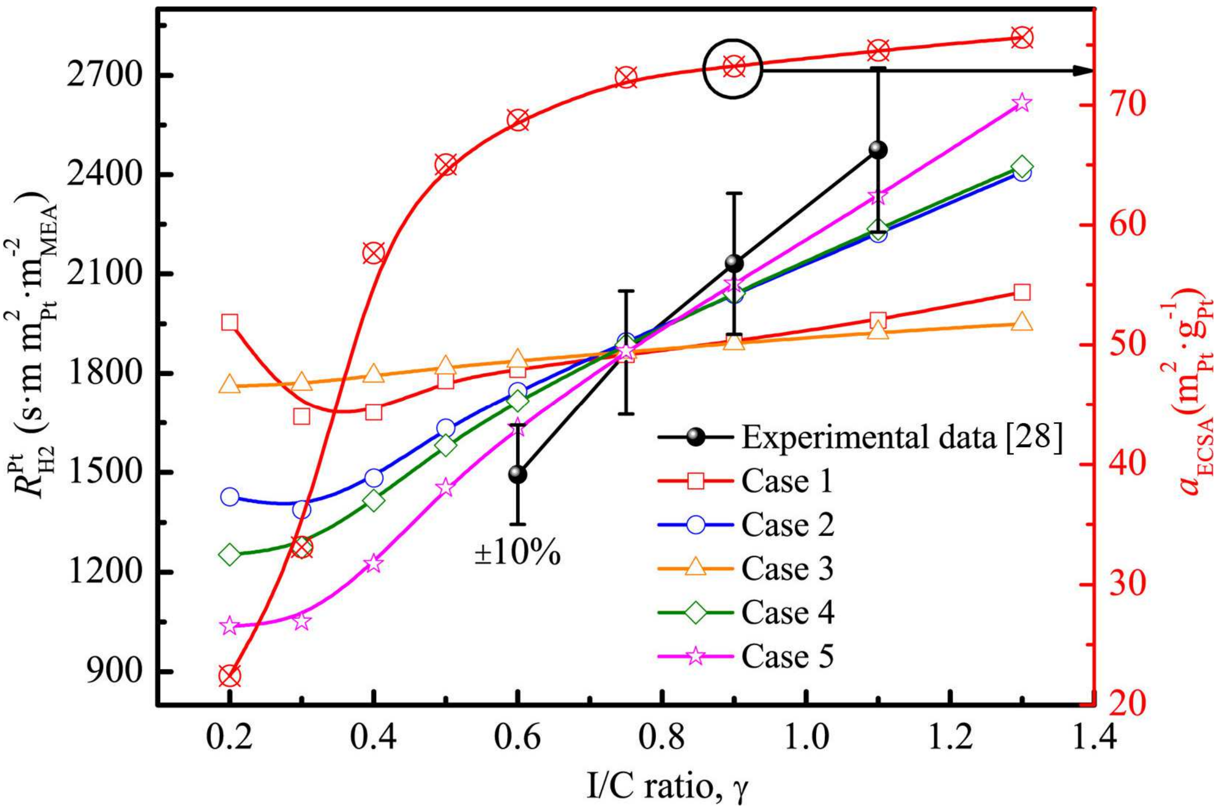

Fig. 7 Local transport resistance $R_{H_2}^{Pt}$ and the mass-weighted electro-chemical surface area a_{ECSA} versus ionomer to carbon ratios γ. Numerical predictions of different cases and the experimental data [28]

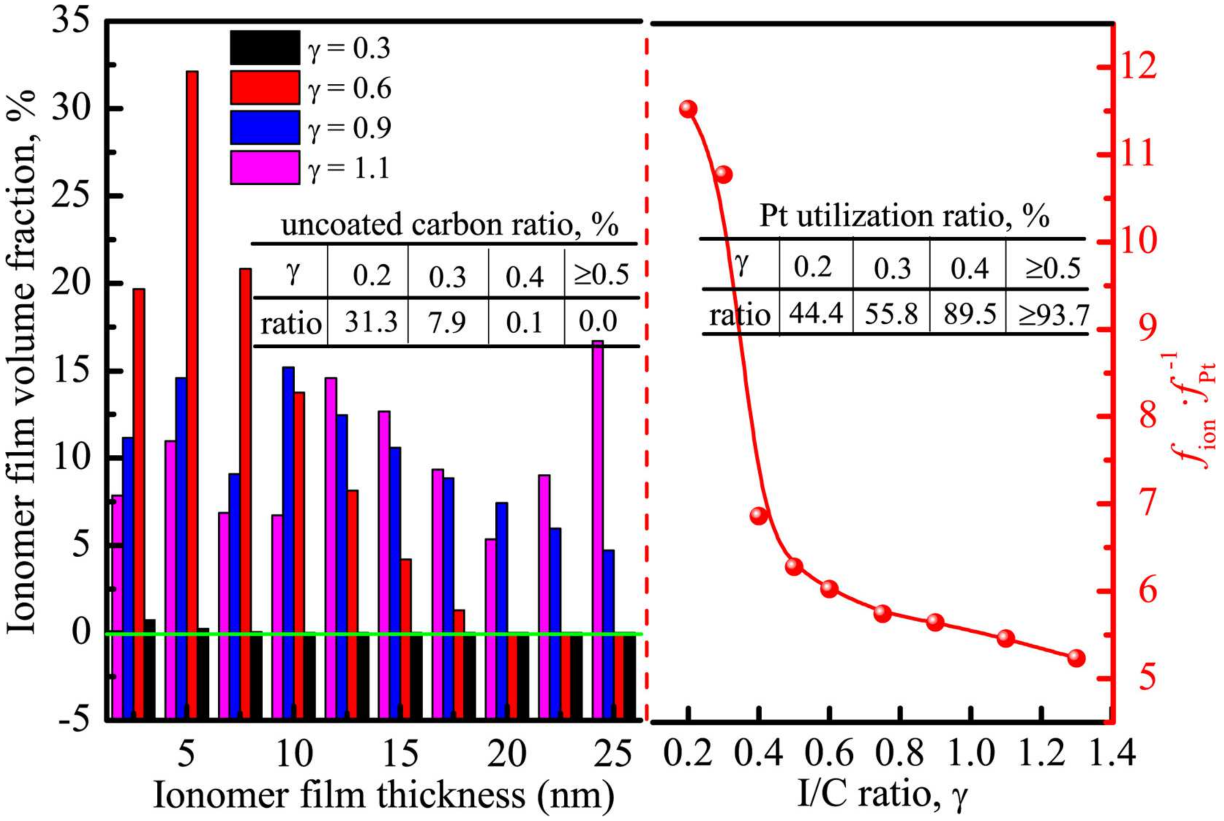

uncoated carbon ratio, %

γ	0.2	0.3	0.4	≥0.5
ratio	31.3	7.9	0.1	0.0

Pt utilization ratio, %

γ	0.2	0.3	0.4	≥0.5
ratio	44.4	55.8	89.5	≥93.7

Fig. 8 Structural parameters of the reconstructed CL for different ionomer to carbon ratio *γ*, left: thin-film volume fraction distribution; right: ratio of f_{ion} relative to f_{Pt}

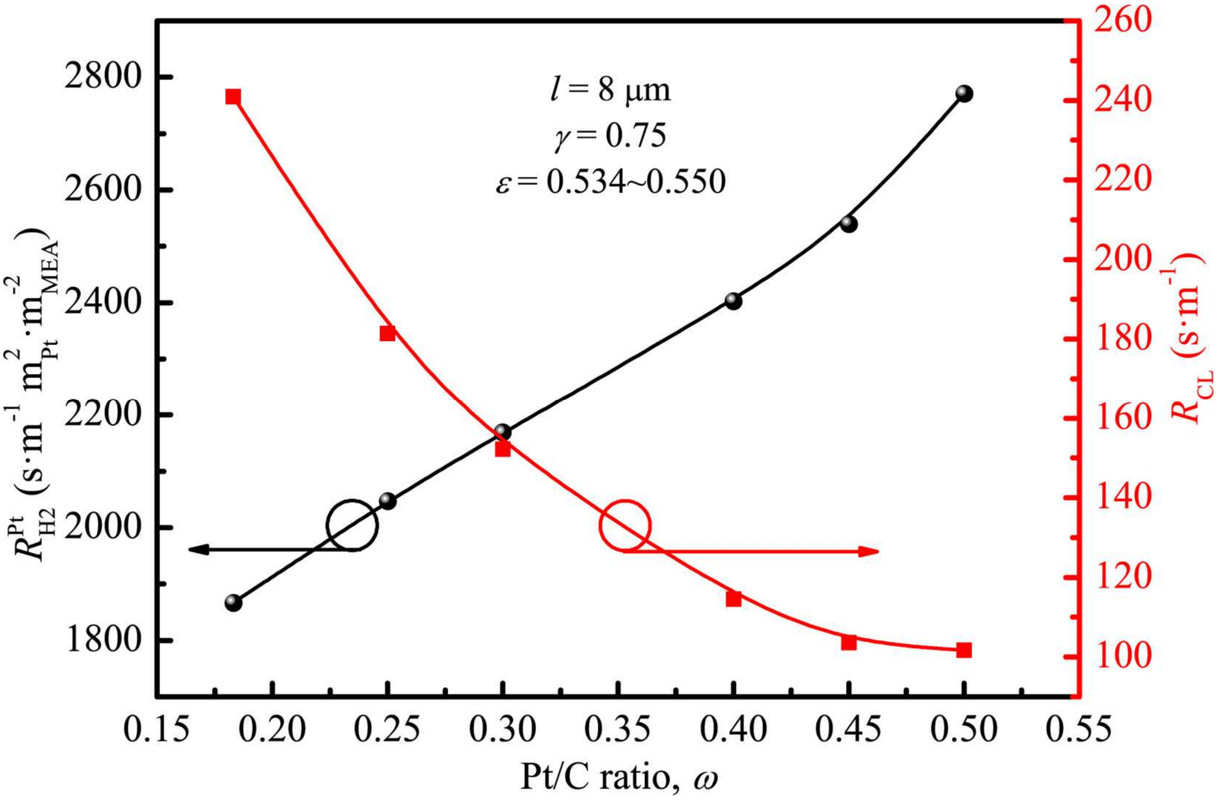

Fig. 9 Variations of the local transport resistance $R_{H_2}^{Pt}$ and R_{CL} with Pt/C ratios, the structural parameters are γ = 0.75 and ε=0.55

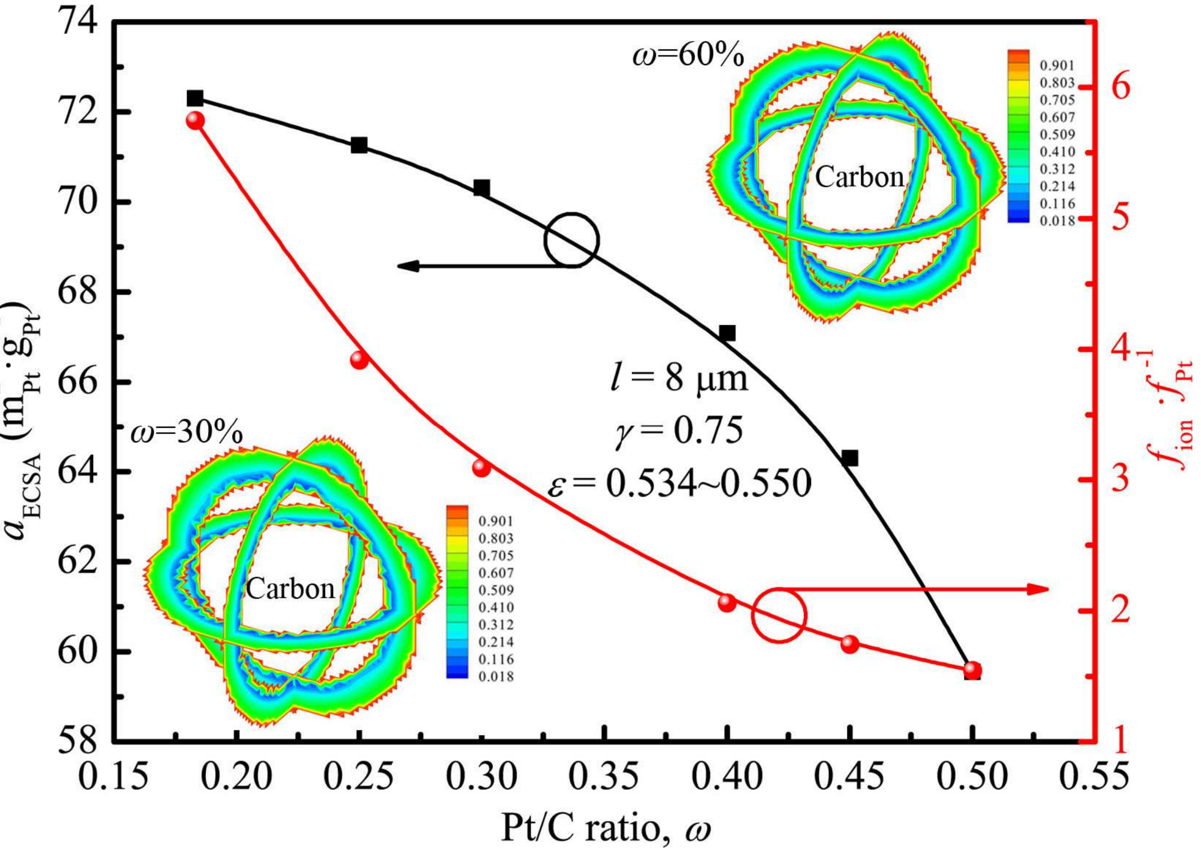

Fig. 10 Variations of the structural parameters a_{ECSA} and the ratio of f_{ion} and f_{Pt} versus Pt/C ratio ω

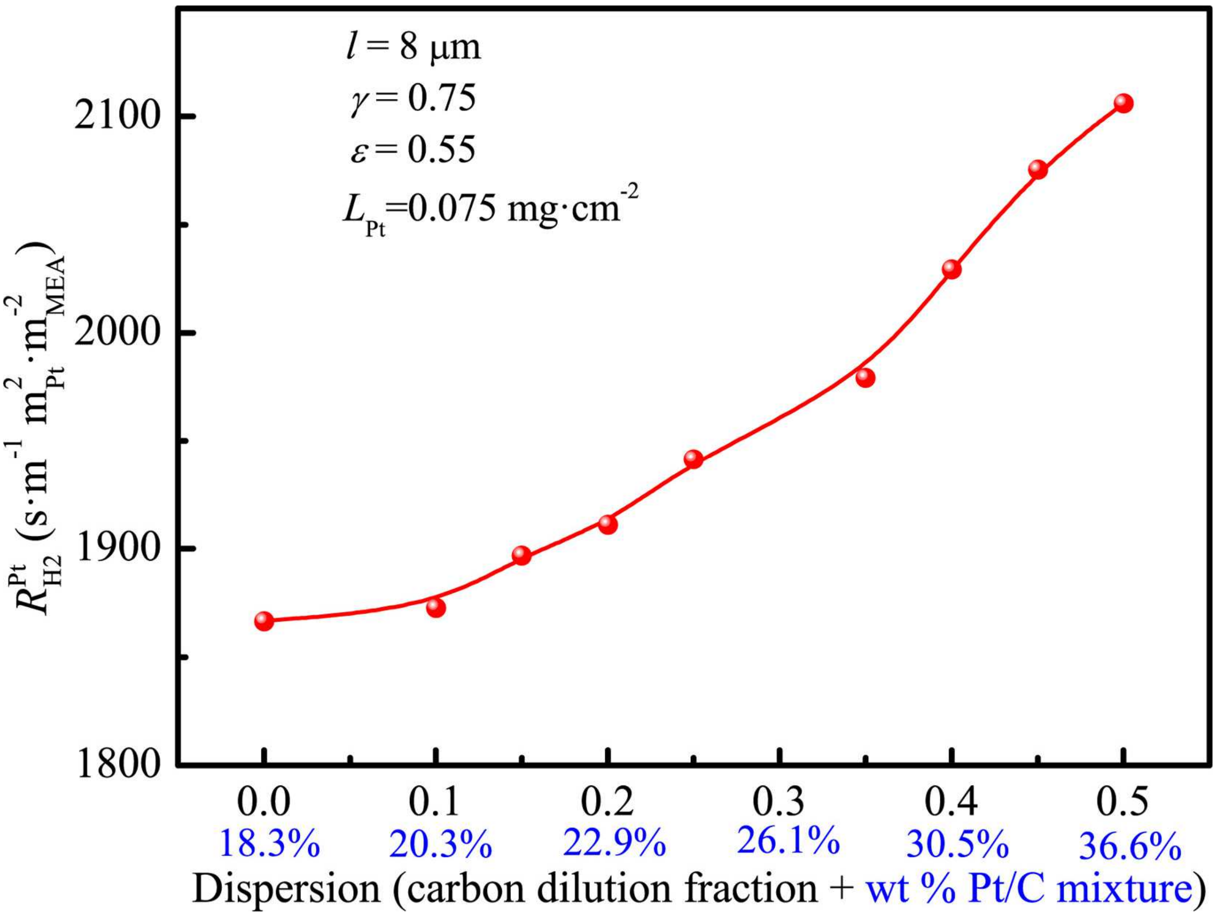

Fig. 11 Variations of the local transport resistance $R_{H_2}^{Pt}$ versus the volume fractions of the bare carbon, ε_{bare}, the structural parameters are γ= 0.75 and ε=0.55, l=8μm

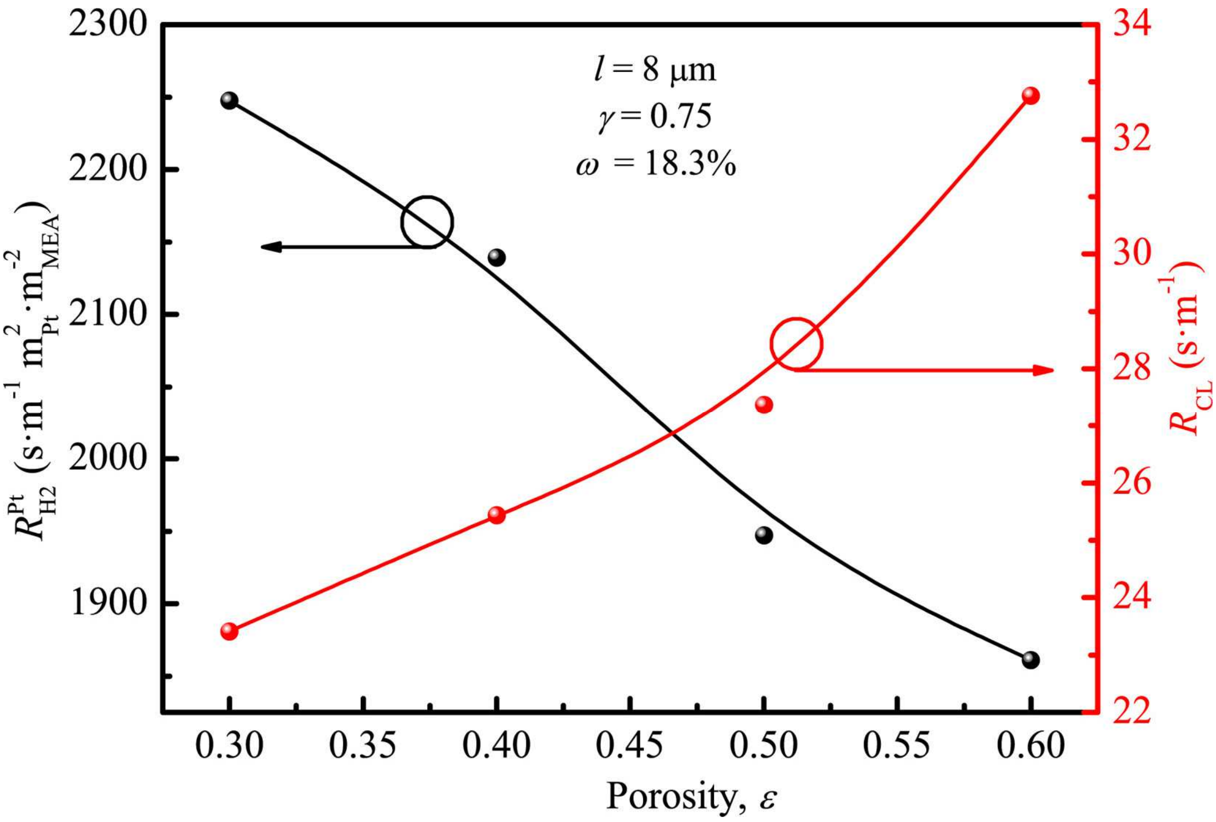

Fig. 12 Variations of the local transport resistance $R^{Pt}_{H_2}$ and R_{CL} with porosity ε, the structural parameters are $\gamma = 0.75$, l =8.0μm and ω=18.3%

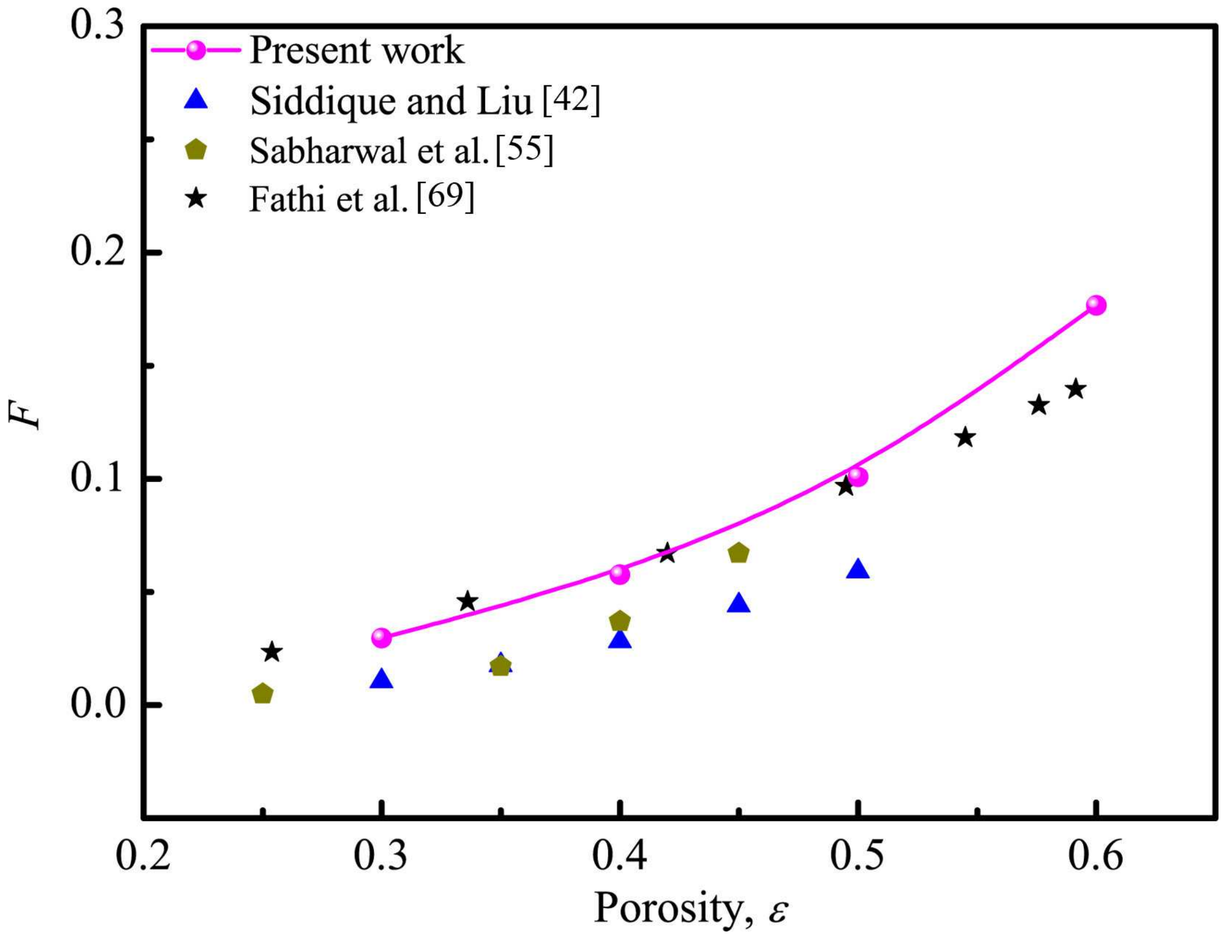

Fig. 13 Comparison of the formation factor with the previously published studies [42, 55, 69]

Table Captions

Table 1 Comparison of the Pt-mass-specific electrochemical surface area a_{ECSA} between the predicted data and the existing experimental data [8, 28, 37]

Table 2 Contribution of the interfacial reaction rates to the local transport resistance $R_{\mathrm{H_2}}^{\mathrm{Pt}}$

Table 3 Comparison of the predicted R_{Pore} with the analytical results for the structural parameters of $\gamma = 0.75$, l =8.0μm, and ω=18.3%

Table 1

Comparison of the Pt-mass-specific electrochemical surface area a_{ECSA} between the predicted data and the existing experimental data [8, 28, 37]

a_{ECSA} Literature	Experimental data ($m^2_{\mathrm{Pt}} \cdot g^{-1}_{\mathrm{Pt}}$)	Numerical data ($m^2_{\mathrm{Pt}} \cdot g^{-1}_{\mathrm{Pt}}$)
Cetinbas et al. [37]	50.0 (1)	51.0
Schuler et al. [28]	73.9 (2)	72.3
Grezler et al. [8]	57.4 (3)	60.7

[1] In Cetinbas et al., the structural parameters of the CL are $\gamma = 0.8$, $\varepsilon = 0.42$, $l = 3.75\mu\mathrm{m}$, $L_{\mathrm{Pt}} = 0.092\ \mathrm{mg}\cdot\mathrm{cm}^{-2}$, ω=30%, Pt-Ni alloy and the mass fraction of Pt is 57%.

[2] In Schuler et al., the structural parameters of the CL are $\gamma = 0.75$, $\varepsilon = 0.55$, $l = 2.8\mu\mathrm{m}$, $L_{\mathrm{Pt}} = 0.03\ \mathrm{mg}\cdot\mathrm{cm}^{-2}$, ω=18.3%, Pt nanoparticle supported on carbon, TEC10E20E, the values are fitted from Table 1 and Fig. 4.

[3] In Grezler et al., the structural parameters of the CL are $\gamma = 0.95$, $\varepsilon = 0.65$, $l = 12.2\ \mu\mathrm{m}$, $L_{\mathrm{Pt}} = 0.4\ \mathrm{mg}\cdot\mathrm{cm}^{-2}$, ω=50%, Pt nanoparticle supported on carbon, TEC10E50E, the value is fitted from Table 2.

Table 2

Contribution of the interfacial reaction rates to the local transport resistance $R_{H_2}^{Pt}$

ψ_0/ψ_{H2} Parameter	1	2.5	5	10	20
k_{ads}^{-1} (s·m^{-1})	1.769	1.838	1.924	2.035	2.158
k_{dis}^{-1} (s·m^{-1})	0.324	0.344	0.371	0.410	0.465

Table 3

Comparison of the predicted R_{Pore} with the analytical results for the structural parameters of $\gamma = 0.75$, l =8.0μm and ω=18.3%

Porosity	0.3	0.4	0.5	0.6
Roughness factor of Pt, f_{Pt} ($\mathrm{m^2 \cdot m^{-2}}$)	101.257	86.253	72.185	57.215
Roughness factor of ionomer, f_{ion} ($\mathrm{m^2 \cdot m^{-2}}$)	433.760	443.425	401.371	347.729
Numerical predicted $D_{\mathrm{H_2}}^{\mathrm{eff}}$ ($\mathrm{m^2 \cdot s^{-1}}$) (1)	2.468E-6	4.793E-6	8.374E-6	1.468E-5
Numerical predicted R_{Pore} ($\mathrm{s \cdot m^{-1}}$)	1.223	0.660	0.384	0.236
Estimated R_{Pore} with Eq. (2), ($\mathrm{s \cdot m^{-1}}$) (2)	1.070	0.554	0.318	0.182
Estimated R_{Pore} with Eq. (3), ($\mathrm{s \cdot m^{-1}}$) (3)	1.081	0.556	0.318	0.182

[1] The effective diffusivity is modeled simply by ignoring the chemical reaction at the Pt surfaces and the proton transport in the ionomer. Hydrogen flux are statically obtained by the given concentration drop at the interfaces of GDL/CL and CL/MEM. The pore size distribution is fully considered and the local diffusivity in the pores is specified with Eq. (9). For details, one can refer to our previous work [52].

[2] The input parameters of $R_{\mathrm{H_2}}^{\mathrm{Pt}}$ and $D_{\mathrm{H_2}}^{\mathrm{eff}}$ to estimate the R_{CL} in Eq. (2) are numerically obtained, and R_{pore} is calculated by subtracting $R_{\mathrm{H_2}}^{\mathrm{Pt}} / f_{\mathrm{Pt}}$ from R_{CL}.

[3] The input parameter of $D_{\mathrm{H_2}}^{\mathrm{eff}}$ to estimate R_{Pore} in Eq. (3) is numerically obtained.